Contributions to Mineralogy and Petrology (2018) 173:24
https://doi.org/10.1007/s00410-018-1452-7

ORIGINAL PAPER

Exhumation rates in the Gran Paradiso Massif (Western Alps) constrained by in situ U–Th–Pb dating of accessory phases (monazite, allanite and xenotime)

Paola Manzotti[1] · Valérie Bosse[2] · Pavel Pitra[3,4] · Martin Robyr[1] · Federica Schiavi[2] · Michel Ballèvre[3]

Received: 6 September 2017 / Accepted: 28 February 2018 / Published online: 2 March 2018
© Springer-Verlag GmbH Germany, part of Springer Nature 2018

Abstract

Exhumation rates for high-pressure metamorphic rocks need to be carefully estimated to decipher tectonic processes in subduction/collision belts. In the Gran Paradiso Massif (Western Alps), the Money Unit crops out as a tectonic window below the Gran Paradiso Unit. According to previous studies, the Gran Paradiso and Money Units reached peak pressure conditions at ~18 to 20 kbar, 480–520 °C and ~17 to 18 kbar, 500–550 °C, respectively. This yields a maximum difference of ~9 to 10 km in the subduction depth reached by these two units during the Alpine history. Thrusting of the Gran Paradiso Unit over the Money Unit led to the simultaneous development of the main foliation under the same metamorphic conditions (~12.5 to 14.5 kbar and 530–560 °C) in both units. The thrust contact was subsequently folded and then both units were exhumed together. The relative timing of the growth and dissolution of the accessory phases was assessed by combining thermodynamic modelling with inclusion, textural and chemical (major and trace element) data from both major and accessory phases. The age of monazite constrained the high-pressure metamorphism in both the Gran Paradiso Unit and the Money Unit at 41.5 ± 0.3 and 42.0 ± 0.6 Ma, respectively. Allanite replacing monazite in the matrix has been dated at 32.7 ± 4.2 Ma. The late growth of xenotime associated with the crystallization of biotite pseudomorphs at the expense of garnet (at about 10 kbar) was dated at 32.3 ± 1.0 Ma. Our petrochronological data indicate about 10 m.y. between the peak pressure conditions and the crystallization of xenotime leading to an exhumation rate of the order of 2.2–5 mm/year. The new ages allow to better constrain the timing of the displacement of the thrust defining the lower boundary of the extruding wedge of eclogite-facies rocks.

Keywords Monazite · Allanite · Xenotime · Exhumation rates · High pressure · Alps

Introduction

Plate tectonics have provided a huge impetus in linking regional structures to larger-scale displacements along plate boundaries (e.g., Argand 1924; Dewey and Bird 1970; Johnson and Harley 2012). However, thermo-tectonic processes in mountain crustal roots, once continental collision has succeeded oceanic subduction, require further clarifications. Analogue and, more recently, numerical models have succeeded in reproducing the main characteristics of the geometrical and kinematical evolution of mountain belts (e.g., Burov et al. 2014). The main strengths of the numerical models are twofold. First, numerical models rely on physically based assumptions about boundary conditions and rheological behaviour for materials involved in the convergence zone. Second, they provide 'synthetic' pressure–temperature–time (*P*–*T*–*t*) paths, which may be compared to the

Communicated by Steven Reddy.

Electronic supplementary material The online version of this article (https://doi.org/10.1007/s00410-018-1452-7) contains supplementary material, which is available to authorized users.

✉ Paola Manzotti
paola.manzotti@gmail.com

[1] Institute of Earth Sciences, University of Lausanne, Géopolis, Quartier Mouline, 1015 Lausanne, Switzerland

[2] Université Clermont Auvergne, CNRS, IRD, OPGC, Laboratoire Magmas et Volcans, 63000 Clermont-Ferrand, France

[3] University of Rennes, CNRS, Géosciences Rennes, UMR 6118, 35000 Rennes, France

[4] Česká geologická služba, Prague 1, Czech Republic

rock record, provided the assumptions used to calculate them are relevant. The best record of the tectonic history in the core of mountain belts can be found in high-pressure (HP) and ultra-high pressure (UHP) metamorphic rocks through their *P–T–t* paths (Andersen et al. 1991; de Sigoyer et al. 2004; Epard and Steck 2008; Yamato et al. 2008; Agard et al. 2009; Kylander-Clark et al. 2012; Warren 2013; Burov et al. 2014). Slices of crustal material have been dragged down into the subduction zone, before detaching from the downgoing slab, and finally being exhumed to the surface. The *P–T* evolution (based on thermodynamic modelling) in time (based on isotopic measurements) must undergo a proper quantitative assessment to have a complete understanding of the tectonic processes leading to the burial and exhumation of crustal slices. In essence, this requires very precise and reliable ages that can be obtained by 'in situ' and 'in context' dating of minerals present in small amounts in many rocks (e.g., monazite, allanite and xenotime). In HP and UHP rocks, these minerals grow well below their closure temperature for intracrystalline diffusion. The timing of their growth, therefore, needs to be carefully assessed with respect to the growth of the major silicates, which are used to determine the *P–T* evolution of the rocks (Kohn et al. 2017). The *P–T–t* path obtained may be related to the rock fabrics that in turn are associated with larger-scale deformations with known geometry and kinematics.

The internal zones of most mountain belts are characterized by a stack of allochthonous units (thrust sheets), each one recording a distinctive *P–T–t* history. The timing of peak *P* (i.e., maximum burial) and the timing of coupling between stacked units (i.e., thrusting) are key parameters for understanding the kinematics of the subduction/collision process. We address this question in one of the best known orogenic belts in the world, the Alps, because the geometry of the nappe stack is well-established. In addition, available *P–T–t* paths were up to now mainly intended to describe the history of individual thrust sheets (e.g., the UHP Brossasco-Isasca Unit: Rubatto and Hermann 2001; the internal Sesia Zone:; Regis et al. 2014a, the oceanic Zermatt Zone:; de Meyer et al. 2014) rather than the evolution of their tectonic boundaries. For this reason, this study focuses on dating the deepest tectonic contact found in the nappe stack of the Western Alps, where higher *P* rocks (Gran Paradiso Unit) are thrusted upon lower *P* ones (Money Unit) (Manzotti et al. 2015a, b). Provided that the age of the peak *P* in the two units and the timing of the thrusting have been determined, then it is possible to establish the timing and rate of the decoupling of crustal slices from the subducting slab during the subduction to collision transition.

Geological setting

The Gran Paradiso Massif in the Western Alps

The Western Alps result from the collision between the European and Adriatic palaeomargins following the subduction of two narrow oceanic domains (Schmid et al. 2004, 2017; Pfiffner 2014). Between the two palaeomargins, some continental ribbons were detached from the adjoining continents, the two main ones being the Sesia-Dent Blanche domain to the east (e.g., Babist et al. 2006; Manzotti et al. 2014a) and the Briançonnais domain to the west (Fig. 1a). The Briançonnais domain was a piece of pre-Triassic crust, on top of which Triassic to Late Eocene sediments were deposited. This piece of crust was subducted below the Piemonte-Liguria Ocean and stacked over the remnants of another ocean basin, located to the west, called the Valaisan Basin.

The most internal units of the Briançonnais microcontinent now crop out as windows below the eclogite-facies meta-ophiolites derived from the Piemonte-Liguria Basin (Fig. 1a). These windows (from south to north: Dora-Maira, Gran Paradiso and Monte Rosa) result from the erosion of antiformal folds affecting the entire crustal wedge during the indentation of the Adriatic mantle (e.g., Schmid et al. 2017). Each window exposes a stack of kilometre-thick basement nappes. In the specific case of the Gran Paradiso Massif (Fig. 1b), two main basement nappes have been defined (Compagnoni et al. 1974; Le Bayon and Ballèvre 2006). The upper one (Gran Paradiso Unit) is essentially made of polycyclic (i.e., recording the Alpine orogenic cycle overprinting a pre-Alpine one) metasediments intruded by Permian granitoids (Bertrand et al. 2005; Ring et al. 2005), now converted into augen-gneisses. These lithologies record eclogite-facies parageneses, partially overprinted by albite–amphibolite facies minerals (e.g., Dal Piaz and Lombardo 1986; Le Bayon et al. 2006; Gasco et al. 2010; Massonne 2015). The lower nappe (Money Unit) consists of a diverse array of monocyclic (i.e., recording only the Alpine orogenic cycle) metasediments and meta-volcanics intruded by the Permian Erfaulet granite (Le Bayon and Ballèvre 2004a, b; Manzotti et al. 2014b). Peak *P–T* conditions were attained at lower *P* compared to the Gran Paradiso Unit (Manzotti et al. 2015b).

Deformation and metamorphic history of the Gran Paradiso Massif

Following previous mapping (Le Bayon et al. 2006; Manzotti et al. 2014a, b), four Alpine evolutionary stages

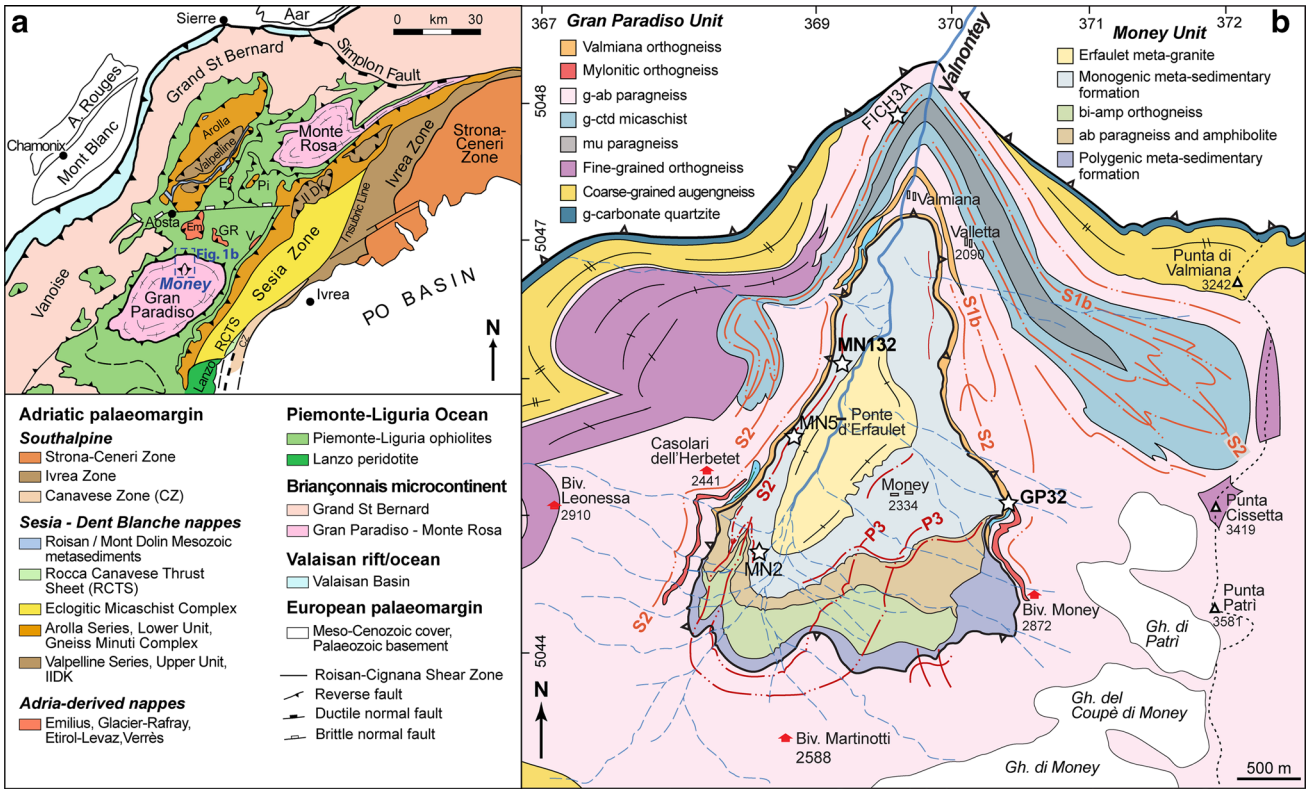

Fig. 1 **a** Simplified map of the Western Alps (Manzotti et al. 2015b). The Gran Paradiso Massif is marked by a white line. *E* Etirol Levaz, *Em* Emilius, *GR* Glacier-Rafray, *Pi* Pillonet. **b** Simplified geological map of the northern sector of the Gran Paradiso Massif (for location see a) showing the Money Unit in the Valnontey valley (Manzotti et al. 2015b). Traces of the foliation (S) and axial plane (P) are represented as red lines. White stars indicate the location of the studied samples. FICH3A is a garnet–chloritoid micaschist studied in Le Bayon et al. (2006)

have been recognized in the Money and Gran Paradiso Units (Manzotti et al. 2015b). In both units, stage 1 is defined by aligned inclusions in garnet cores, or microfolded schistosities preserved in narrow microlithons (S_1). Following the detailed petrological investigation of Manzotti et al. (2015b), these features record late prograde and peak *P* assemblages, attained in eclogite- (~ 18 to 20 kbar, 480–520 °C) and blueschist-facies (~ 17 to 18 kbar, 500–550 °C) conditions in the Gran Paradiso and Money Units, respectively.

Stage 2 is responsible for the development of the dominant foliation (S_2) in both units, and is parallel to lithological boundaries inside the main units and to the contact between the Gran Paradiso and Money Units. This stage took place at similar *P*–*T* conditions in both units, i.e., in the albite stability field at relatively high *P* (~ 12.5 to 14.5 kbar and ~ 500–540 °C; Manzotti et al. 2015b). The dominant foliation S_2 is, therefore, associated with the thrusting of the Gran Paradiso Unit onto the Money Unit.

Field observation and structural data show that the thrust contact was deformed by kilometre-scale folds (see Manzotti et al. 2014a, b for further details) (stage 3), locally associated with a crenulation cleavage (S_3) overprinting S_2. A late, static retrogression (stage 4) occurred under greenschist-facies conditions.

Based on the peak *P* difference between the two stacked units (i.e., 1–5 kbar), the distance of the vertical component of the displacement along the thrust is estimated to be ~ 3 to 15 km (Manzotti et al. 2015b). This value only represents part of the total displacement along the thrust, as the horizontal component depends on the dip of the thrust plane, which is unknown. This conclusion relies on the assumption that both units were subducted at the same time, a reasonable assumption considering that the Gran Paradiso Unit represents the leading edge of the subducting continental crust, and the Money Unit is a more proximal part of the same crustal slab. Previous studies have attempted to establish the age of the HP event in the Gran Paradiso Unit (see the following section), but no radiometric data for the Money Unit are available so far. The goal of our isotopic work (i.e., U–Th–Pb dating of monazite, allanite and xenotime) is to clarify the timing of these metamorphic stages.

Previous geochronological work in the Gran Paradiso Massif

Meffan-Main et al. (2004) proposed an age of 43.0 ± 0.4 Ma for the HP stage in the Gran Paradiso Unit. This age is based on a Rb–Sr microsample of an apatite–phengite pair in a Mg-rich micaschist (the so-called silvery micaschists or whiteschists). According to the SHRIMP study by Radulescu et al. (2009) on another sample of the silvery micaschists, prograde monazite yielded an age of 37.4 ± 0.9 Ma and peak *P* allanite yielded an age of 33.7 ± 1.6 Ma. Based on a range of ages provided by the Rb/Sr and Ar/Ar methods on carefully selected shear zones in the orthogneisses, Rosenbaum et al. (2012) proposed that peak *P* metamorphism took place near 41 Ma and prior to 39 Ma. Note that the discrepancy between the different sets of data for the HP stage is of the order of 10 Ma.

Previous studies also tried to date the "greenschist-facies" overprint in the Gran Paradiso Unit. For Meffan-Main et al. (2004), the overprint took place at 36.3 ± 0.4 Ma (Rb–Sr), probably in the 36–34 Ma interval. Rosenbaum et al. (2012) provided a range of ages from 39.2 ± 0.4 to 33.3 ± 0.4 Ma for different cleavage domains, indicating exhumation within a range of 41–34 Ma.

Finally, fission-track data on zircon (c. 33–30 Ma) and apatite (c. 24–11 Ma) provide constraints on the latest steps of the exhumation history of the Gran Paradiso Massif (Hurford and Hunziker 1989; Malusà et al. 2005; Malusà and Vezzoli 2006).

The main goal of this study is to provide geochronological data for constraining large-scale tectonic processes, i.e., the timing of the HP metamorphism and the rate of exhumation of the most internal part of the Briançonnais micro-continent. In this respect, our approach slightly differs from the one used in published works. For instance, previous studies have attempted to either constrain the age of the high-*P* event using the best preserved HP parageneses (e.g., Meffan-Main et al. 2004; Radulescu et al. 2009) or to date specific shear zones, the kinematics of which could be linked to the exhumation history (Rosenbaum et al. 2012). Despite the value of these two approaches, our study aims to date accessory minerals that can be related to specific fabrics and metamorphic stages (if possible within a single sample), that are linked to mapped larger-scale structures. To achieve this goal, the textural, chemical and isotopic record of the accessory phases was directly investigated in thin sections. The first target of our isotopic work is to establish the age of the peak *P* stage in each unit (i.e., the Gran Paradiso and Money Units) to clarify the relative timing of the subduction of these two units. The second target is to establish the timing of the thrusting of the Gran Paradiso Unit over the Money Unit, a topic that has never been addressed in previous works.

Methods

Sampling strategy

Our previous petrological study in the Gran Paradiso Unit (sample GP32, Manzotti et al. 2015b) constitutes a robust basis for a geochronological investigation of the same sample. Sample GP32, a garnet–chloritoid micaschist, was collected on the right side of the Valnontey valley (Fig. 1b and S1a, b in the electronic supplementary material, hereafter called ESM), as close as possible to the tectonic boundary with the Money Unit (i.e., ~3 to 4 m above).

The *P*–*T* history of the Money Unit has been previously described based on the detailed study of a meta-conglomerate (sample MN2, Manzotti and Ballèvre 2013; Manzotti et al. 2015b). Unfortunately, this sample (MN2) cannot be used for geochronology due to the lack of accessory U–Th-bearing phases. Consequently, another sample (i.e., MN132) from the same unit was chosen. It is a garnet–albite-bearing micaschist, collected on the left flank of the Valnontey valley, in the monogenic meta-sedimentary formation, north of the Pont des Erfaulets (Fig. 1 and S1c).

Textural and petrographical investigations

All samples were analysed in thin sections to link the chemistry and U–Th–Pb dates to the metamorphic assemblages and structures. Textures of the accessory phases and their relation to the rock fabrics were studied by optical petrography in polished thin sections and back scattered electron (BSE) imaging by scanning electron microscopy ("Imaging and electron probe microprobe analysis" paragraph in the ESM). Inclusions in accessory minerals (i.e., monazite) have been carefully examined using back-scatter electron imaging, energy dispersive spectroscopy (EDS) and Raman spectroscopy for phase identification. The chemical composition (major and trace elements) of the accessory phases and major minerals was systematically studied by electron probe microanalyzer (EPMA) chemical mapping and analysis and by in situ LA-ICP-MS analysis. Mineral abbreviations and symbols used in this study are listed in Table S1 of the ESM.

Whole-rock chemistry

Major and minor elements were determined in whole-rock samples (GP32B and MN132) by ICP-AES and incompatible trace elements were determined by ICP-MS (CRPG, Nancy; Tables S2 and S3, Fig. S2). Bulk-rock glasses were prepared by mixing appropriate proportions (1:5) of fine-grained rock powder with di-lithium tetraborate. Details

about the method used for the analyses are available in Carignan et al. (2001).

The system compositions (SC) (for major elements) of sample GP32 (type-I and type-II domains, see below) used for phase diagram calculations were obtained by the area-scan method using SEM-EDS (JSM-7100F scanning electron microscope, University of Rennes 1) on domains measuring ~ 4 × 3 mm (see Groppo et al. 2006, 2009a, b; Manzotti et al. 2015b for similar methods and further details). The area size and location were chosen considering the occurrence of stable minerals during the metamorphic stage of interest. Two system compositions were measured for the type-I domain (sample GP32): one on an area including entire garnet porphyroblasts, and another on part of the same area but excluding garnet cores. The amount of Ca was corrected for the presence of apatite using the analysed amount of phosphorous (with the exception of sample GP32B (type-II domain), where the amount of phosphorous is related to the presence of xenotime). To sum up, we modelled four system compositions, i.e., SC1 (i.e., GP32B type-I domain, including full garnet, same as Manzotti et al. 2015b), SC2 (GP32B type-I domain, excluding garnet cores), SC3 (i.e. GP32 type-II domain) and SC4 (MN132).

Phase diagram calculations

Phase relations were modelled in the chemical system $MnO–Na_2O–CaO–K_2O–FeO–MgO–Al_2O_3–SiO_2–H_2O–TiO_2–Fe_2O_3$ (MnNCKFMASHTO). Given the pelitic character of the samples, the amount of Fe^{3+} was set to 5% of total Fe ($X(Fe^{3+}) = Fe^{3+}/Fe_{total}$), an arbitrary low value. Several P/T-$X(Fe^{3+})$ pseudosections were calculated to check how sensitive the results are to this choice. Variations of $X(Fe^{3+})$ in the range 0–10% have limited effects on the position of most equilibria, with the exception of the relative stability of rutile, ilmenite and magnetite.

Isochemical phase diagrams (pseudosections) were calculated with the Theriak/Domino software (de Capitani and Brown 1987; de Capitani and Petrakakis 2010) and Thermocalc software (Powell and Holland 1988) using, in both cases, the internally consistent thermodynamic data set 5.5 (Holland and Powell 1998; updated November 2003) and identical mixing models for solid solutions. Additional information on the solid solution models, the chemical system used and the phases considered in the calculations are presented in the ESM (paragraph Phase diagram calculations). It is worth emphasizing that the phase diagrams calculated with either Theriak/Domino or Thermocalc gave the same results as the same thermodynamic dataset and same solid solution models were used.

The pseudosection modelling results were complemented using empirically (Fe–Mg partitioning between garnet and chloritoid: Perchuk 1991) or experimentally calibrated (Ti content in biotite: Henry et al. 2005) thermometers. In addition, the maximum T in the studied samples was checked independently using Raman spectroscopy on carbonaceous material (RSCM, Beyssac et al. 2002). Raman spectroscopy on quartz inclusions in garnet was performed to estimate the entrapment P of these inclusions (using the calibration of Ashley et al. 2014). This method (based on the elastic properties of inclusions and their host) allows an estimation of P which is independent from the equilibrium thermodynamics approach used by Theriak/Domino or Thermocalc.

Geochronology

Accessory phases (allanite, monazite, xenotime) were dated by LA-ICP-MS in situ U–Th–Pb analysis on polished thin sections. Geochronological analytical methods are presented in detail in the ESM. Monazite can be dated using both U–Pb and Th–Pb decay schemes. In this study, only $^{232}Th–^{208}Pb$ ages and uncertainties ($\pm 2\sigma$) were considered for the following reasons. First, ^{232}Th is largely predominant in monazite, allowing small spots to be performed during laser ablation. Second, U decay series could be in disequilibrium in young monazites (Schärer 1984) resulting in the overestimation of the $^{206}Pb/^{238}U$ ages. Because secular equilibrium among the intermediate daughters of ^{232}Th occurs after roughly 30 years, it seems reasonable to assume that initial ^{208}Pb is absent. Third, ^{232}Th is so abundant that ^{208}Pb originating from common Pb is usually negligible compared to radiogenic ^{208}Pb. However, to overcome the effect of possible common Pb contamination, we first took the ages that were concordant in the $^{208}Pb/^{232}Th–^{206}Pb/^{238}U$ diagram into account in the calculation (Tables S5 and S8). Assuming a reasonable value for the $^{207}Pb/^{206}Pb$ ratio of common Pb at 42 Ma ($^{207}Pb/^{206}Pb = 0.838$; Stacey and Kramers 1975), we were able to estimate common Pb contamination in the monazite. Following this procedure, we only considered $^{208}Pb/^{232}Th$ ages corresponding to less than 20% of common Pb (Tables S5 and S8) in each sample.

Results for the Gran Paradiso Unit

Petrography (sample GP32)

Sample GP32 has been cut perpendicular to the foliation, and both parallel (GP32A, Fig. S4) and perpendicular (GP32B, Fig. S5) to the stretching lineation. In both cases, two thin sections were studied to detect a sufficient number of monazite, allanite and xenotime crystals. Table S9a summarizes the deformation/mineral growth relationships of sample GP32. Based on differences in the mineral assemblages, two types of domains can be distinguished (Fig. S5), which may represent former lithological

layering, now parallel to the S_1 foliation (Fig. S5). The type-I domain (sample GP32A and part of sample GP32B) preserves the S_1 foliation, marked by white mica, chloritoid and rutile (stage 1). The S_1 foliation is crenulated during stage 2 leading to the development of the main foliation S_2, a crenulation cleavage defined by chloritoid, white mica, ilmenite, and locally, chlorite. Quartz, chloritoid and rutile form inclusions in garnet porphyroblasts (0.5–1 cm). Chlorite aggregates develop later, crosscutting both S_1 and S_2 and replacing garnet. The type-II domain (part of sample GP32B) is dominated by biotite, quartz ± chlorite. The main difference between type-I and type-II domains is that biotite (X_{Mg} = 0.24–0.27; Ti = 0.16–0.20 p.f.u., Table S10), instead of chlorite, replaces garnet porphyroblasts in the type-II domain, whereas it is very poorly developed in the type-I domain. Because the shape of the pseudomorphs after garnet is well-preserved, whereas stage 2 is associated with a penetrative ductile deformation, the pseudomorphs must have developed after stage 2. Some biotite crystals also form aggregates crosscutting the main foliation.

Garnet chemistry

In sample GP32, garnet occurs as polygonal (Fig. 2) or rounded porphyroblasts (0.5–1 cm) wrapped by the S_2 foliation. Garnet is almandine-rich and displays a significant decrease in grossular (from 21 to 6 mol%) and spessartine (from 16 to 2 mol%) from core to rim, balanced by an increase in almandine (from 62 to 84 mol%) and pyrope (from 2 to 7 mol%). X_{Fe} decreases smoothly from 0.96 to 0.92 from core to rim (Fig. 2). In detail, the grossular content displays a plateau or a slight increase (16–21 mol%) in the core, whereas spessartine continuously decreases (16–6 mol%). In the inner rim, grossular strongly decreases (21–10 mol%), then slowly decreases (10–6 mol%) in the outer rim, whereas spessartine continues to regularly decrease (6–2 mol%) throughout both the inner and outer rim (Table S10). Garnet displays trace element zoning (Fig. 2c; Table S11): the Y and M-HREE contents decrease from core (Y ~ 3000 ppm, Dy_N/Yb_N = 0.1–1.0) to rim (Y ~ 130 ppm, Dy_N/Yb_N = 1.7–7.3). Quartz (largely dominant), allanite, rutile, chloritoid and apatite occur as randomly oriented inclusions in garnet cores (stage 1; Fig. 2). Occasionally, quartz grains are roughly aligned parallel to the crystal faces of the garnet (Fig. 2a, d), mimicking the incremental growth stages of garnet. Garnet rims contain rare inclusions of monazite (Fig. 2e).

P–T results

In our previous work (Manzotti et al. 2015b), the *P–T* history of the early Alpine evolution of the Gran Paradiso Unit (stages 1 and 2) was modelled using the bulk composition of the type-I domain of sample GP32B (i.e., SC1) and systematically considering H_2O in excess. *P–T* conditions have been estimated at ~ 18 to 20 kbar, 480–520 °C (stage 1) and at ~ 12.5 to 14.5 kbar and ~ 500 to 540 °C (stage 2).

Contrasting mineral assemblages developed during the late *P–T* evolution of the studied Gran Paradiso sample in the type-I and type-II domains. In the type-I domain, the mineral assemblages developed during stages 1 and 2 are well-preserved and the garnet porphyroblasts are only partially replaced by chlorite. The inferred *P–T* path (Fig. 11 in Manzotti et al. 2015b) displays a sub-isothermal decompression at ~ 540 °C. To explain the textural differences and to further constrain the previously obtained findings, we provide three new results in this study. First, the sub-isothermal position of the garnet mode isopleths calculated for SC1 with H_2O in excess (Fig. 3a) explains the observation that garnet is not dissolved during decompression (from 20 to 12–14 kbar, between stages 1b and 2) in the type-I domain along the proposed *P–T* path. Note that this conclusion has been obtained under H_2O-saturated conditions, not necessarily achieved during decompression, but which are the most favourable for promoting garnet dissolution. Second, a maximum *T* of 526 ± 30 °C that we calculated for the type-I domain using the Raman Spectroscopy of Carbonaceous Material (RSCM, Beyssac et al. 2002, 2003), is in agreement with the *T* estimated in our previous phase diagram calculation (Manzotti et al. 2015b). Third, we show that the effect of garnet fractionation is negligible. SC2 (obtained by removing garnet cores from SC1) has a smaller amount of Ca and Mn that are preferentially sequestered in garnet cores. However, the pseudosection (Fig. S6) calculated using SC2 (and H_2O in excess) shows very little difference with respect to the one calculated using SC1. The fields for mineral assemblages are the same, and the isopleths for the garnet and chloritoid composition are slightly changed (e.g., a decrease of about 10 °C for Grs10), well within the uncertainties associated with the solid solution models.

Bulk composition: type-I vs. type-II domains

In the type-II domain (only present in part of sample GP32B, Fig. S5), crystallization of biotite and resorption of garnet have been observed, suggesting decompression and equilibration in biotite-bearing fields. The Ti content in biotite (Ti = 0.16–0.20 p.f.u.) from this domain corresponds to a crystallization *T* of 491–552 °C (± 24 °C, using Henry et al. 2005). Therefore, the *T* range obtained in both domains suggests that decompression was not accompanied by substantial heating (*T* of stage 2 ~ 500 to 540 °C), as already reported for the Gran Paradiso Massif by Le Bayon et al. (2006).

The different mineral assemblages observed in the two domains, and specifically the diverse degree of overprint

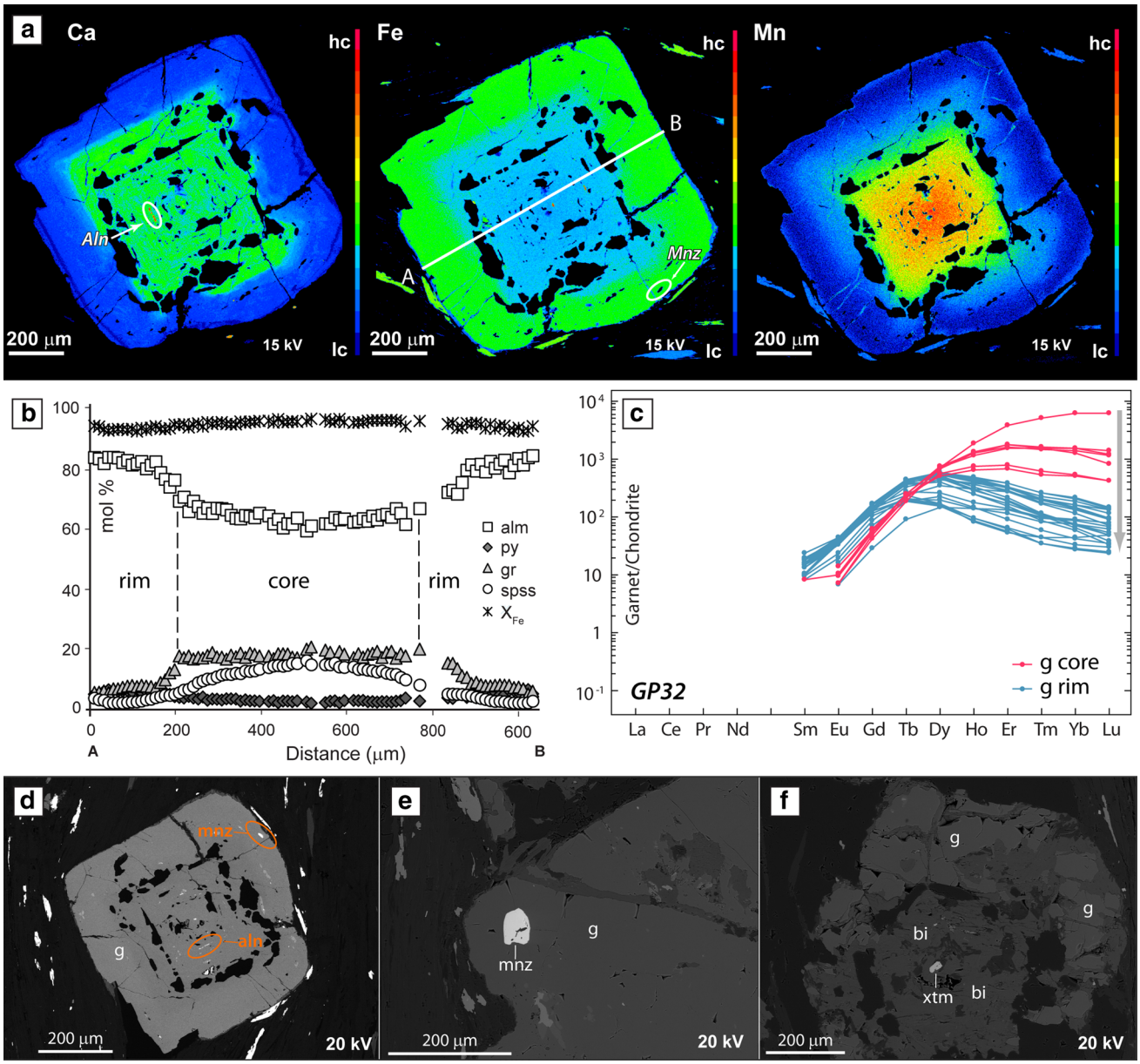

Fig. 2 Garnet chemistry from sample GP32 from the Gran Paradiso Unit. **a** X-ray mapping images of a garnet porphyroblast (*hc* high concentration, *lc* low concentration). Allanite occurs in the garnet core, whereas monazite is found in the rim (see also Fig. 3b). **b** Compositional profile of garnet along the white line A–B traced in (**a**). **c** Garnet REE plot, normalized to chondrite values of Sun and McDonough (1989). **d** Garnet porphyroblasts displaying allanite inclusions in the core and monazite inclusions at the rim, **e** Monazite included at the rim of a garnet porphyroblasts, **f** Biotite and xenotime replacing garnet

during decompression, may result from differences (1) in their primary bulk composition (Fig. S2a) or (2) in their H_2O content. Indeed, H_2O availability plays a major role in the reaction kinetics during *P–T* evolution involving cooling and strongly influences the phase equilibria and thus *P–T* estimates (e.g., Guiraud et al. 2001; Proyer 2003; Le Bayon et al. 2006; Pitra et al. 2010). The first hypothesis (i.e., the role of differences in bulk chemistry) was explored by calculating *P–T* pseudosections in the ranges of 4–12 kbar and 400–600 °C, using two different system compositions, one of which corresponds to type-I (i.e., SC1, already used in Manzotti et al. 2015b; Fig. 3) and the other to type-II (i.e., SC3; Fig. 4) domains. The fluid phase was fixed as pure H_2O, initially in excess (Figs. 3b, 4a). To test the second hypothesis (i.e., the role of a possible difference in H_2O content between the two domains), the *P–T* pseudosections were recalculated with a fixed amount of H_2O (Figs. 3c, d, 4b). This amount was determined, so that the proportion

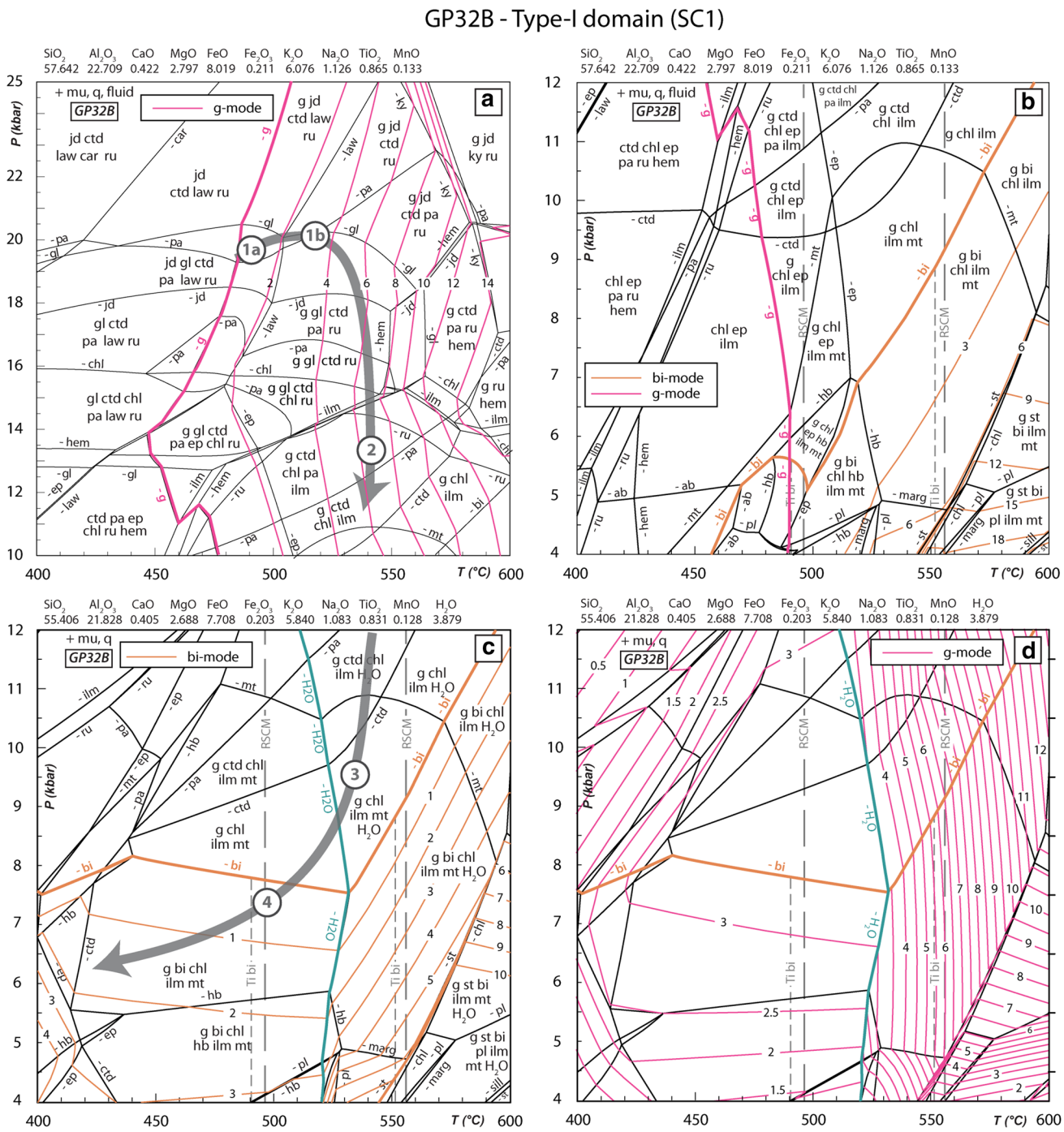

Fig. 3 *P–T* pseudosections calculated for the garnet–chloritoid micaschist (sample GP32, Gran Paradiso Unit) using the system composition of the type-I domain (see Fig. S3). **a** *P–T* pseudosection (in the range 10–25 kbar and 400–600 °C) with H_2O-saturated conditions and contoured for the garnet modal amount (vol%) (see Manzotti et al. 2015a, b for details on the *P–T* path reconstruction). The grey arrow indicates the *P–T* path (stages 1a, 1b, and 2) consistent with mineral assemblages and their chemical composition. **b** *P–T* pseudosection (in the range 4–12 kbar and 400–600 °C) under H_2O-saturated conditions. **c** *P–T* pseudosection for a fixed amount of H_2O, contoured for the garnet modal amount (vol%). The grey arrow indicates the *P–T* path (stages 3 and 4) consistent with mineral assemblages. **d** The same pseudosection as **c** contoured for the biotite modal amount (vol%). Some fields are not labelled for the sake of clarity; their assemblages can be deduced from assemblages in adjacent fields. *T* estimates, using RSCM (grey fine dashed line), and the Ti content in biotite (grey thick dashed line) are reported in **b–d**

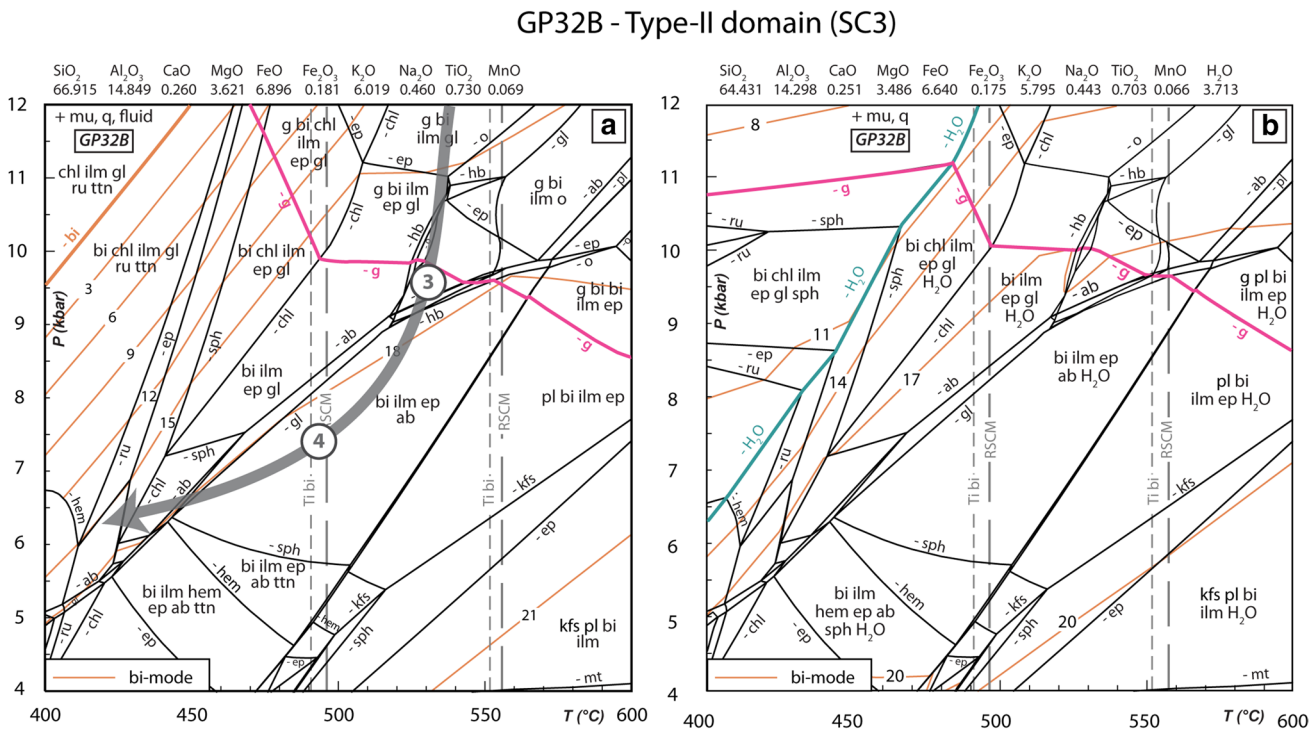

Fig. 4 *P–T* pseudosections calculated for the garnet–chloritoid micaschist (sample GP32, Gran Paradiso Unit) using the system composition of the type-II domain (see Fig. 3). The results for the RSCM (grey fine dashed line) and Ti content in biotite (grey thick dashed line) are also reported. **a** H_2O-saturated conditions. The grey arrow indicates the *P–T* path (stages 3 and 4) consistent with mineral assemblages. **b** Diagram calculated for a fixed amount of H_2O and contoured for the biotite modal amount (vol%). Some fields are not labelled for the sake of clarity; their assemblages can be deduced from assemblages in adjacent fields

of the free fluid phase in the rock does not exceed 1 vol.% (Thompson and Connolly 1990) at peak *T* (inferred from Figs. 3a, 4a).

Compared to the *P–T* pseudosection calculated for type-I (Fig. 3b), the type-II domain bulk composition (Fig. 4a) results in (1) the absence of garnet at low *P* (< 9 to 10 kbar at 500–550 °C), (2) the absence of chlorite at high *T*, and (3) the stabilization of biotite towards high *P* at low *T*. Biotite mode isopleths of biotite mode suggest that, with the bulk composition of the type-I domain (SC1), only a limited amount of biotite (~ 3 to 6 vol.%) developed during cooling and decompression (at *T* < ~ 550 °C, Fig. 3c). By contrast, a large amount of biotite (up to 21 vol.%) forms with the type-II domain composition (SC3, Fig. 4b).

Role of H_2O saturation

The H_2O-saturation surface (blue line in Figs. 3c, d, 4b) divides the pseudosections into a H_2O-saturated part at high *T* and a H_2O-undersaturated part at low *T*. In the pseudosection calculated with the type-I domain system composition (SC1, Fig. 3c, d), the H_2O-saturation limit is nearly isothermal, located at 520 °C at 4 kbar and at ~ 515 °C at 12 kbar. Therefore, a *P–T* evolution involving cooling would rapidly result in fluid-absent conditions, rendering a complete re-crystallization of the rock difficult. Compared with the pseudosection of Fig. 3b calculated with the same bulk composition, H_2O-undersaturated conditions result in the absence of epidote and the stabilization of biotite towards low *T* (at *P* < 8 kbar, Fig. 3c, d). The mineral assemblages observed in type-I domain, and the preservation of garnet, strongly suggest H_2O-undersaturation during decompression.

In the pseudosection calculated for the type-II domain (Fig. 4b), the H_2O-out line has a positive slope and goes from 400 °C and ~ 6.5 kbar, to 490 °C and ~ 12 kbar. This implies that the late *P–T* evolution of the type-II domain occurred under fluid-present conditions, despite the lower proportion of H_2O in the bulk composition (with respect to SC1), resulting in the extensive replacement of garnet by biotite. As both type-I and type-II domains follow the same *P–T* path, the difference in the degree of H_2O saturation explains the contrasting amount of retrogression developed during decompression by the two domains.

To conclude, the difference in mineral assemblages and degree of re-crystallization during decompression observed between the type-I and type-II domains reflect a difference in their bulk composition. The growth of chlorite requires significant amounts of H_2O, leading rapidly

to H_2O-undersaturated conditions, halting further chlorite crystallization and consequently limiting retrogression. On the other hand, in the less aluminous type-II domain, biotite instead of chlorite crystallises during decompression. The lower amounts of structurally bound H_2O sequestered in biotite allow significant quantities of biotite to crystallise, while preserving H_2O-saturation. These conditions favour significant retrogression.

Textural characteristics and chemical composition of accessory phases

Samples GP32 contain four U–Th-bearing accessory phases, namely monazite, allanite, xenotime and apatite.

Monazite distribution and textural relationships

In samples GP32, monazite grains (total $n = 112$) occur in the matrix and as inclusions in garnet, ilmenite and apatite. In sample GP32B, monazite crystals occur in the type-I domain, whereas they are rare in the type-II domain. The shape of the grains varies mainly as a function of their textural position. Two groups of monazite (Table S12) have been identified on the basis of their textural settings, monazite inclusions (group 1) and matrix monazite (group 2).

Monazite inclusions (group 1) are relatively rare. Thirteen prismatic elongated or rarely sub-rounded inclusions (~25 to 100 µm) were found in garnet, always in the outermost low-Ca domains of the porphyroblasts (Figs. 2d, e, 5a), whereas allanite was found in the garnet core (Figs. 2d, 7a). In garnet partially replaced by chlorite at the rim, monazite crystals display internal straight, sharp and well-defined boundaries with garnet (indicating simultaneous crystallization) (Vernon 2004) and external irregular and resorbed grain boundaries with chlorite (Fig. 5a). One elongated prismatic inclusion (~30 µm) with straight grain boundaries was found in ilmenite and one in apatite, one rounded inclusion (10 µm) in ilmenite.

Matrix monazite (group 2) is common. It forms prismatic, elongated crystals, oriented either parallel to or at a high angle with respect to the S_2 foliation. The latter (~20 to 80 µm) ($n = 20$) appear physically corroded and frequently show deeply indented boundaries. Some grains are partially replaced by allanite or by a fine mixture of apatite and allanite and they are often found in association with ilmenite.

Crystals aligned parallel to the S_2 foliation (~20 to 100 µm) ($n = 70$) are locally associated with ilmenite. Some crystals display straight grain boundaries, while other ones have irregular and embayed boundaries and they are partially replaced by allanite at their rims. Rare irregular grains ($n = 6$) (30–90 µm) occur in association with albite or chlorite aggregates; the latter replaces garnet.

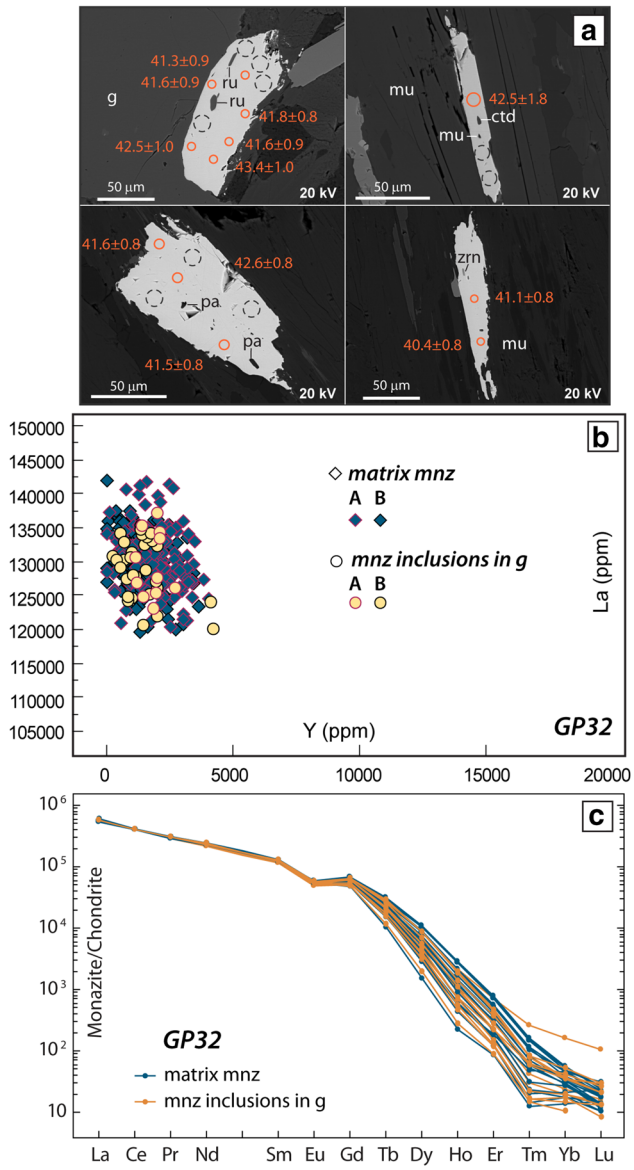

Fig. 5 Textural characteristics and chemical composition of monazite from the Gran Paradiso Unit. Analysed spots are indicated by orange circles (diameter: 7 and 9 µm) for isotopic dating and by dashed grey circles (diameter: 15 µm) for REE. The numbers indicate the $^{208}Pb/^{232}Th$ ages in Ma with 2 σ error. **a** BSE images of matrix monazite and monazite included in garnet. Monazite grains display inclusions of rutile, paragonite, Si-rich muscovite, chloritoid and zircon. **b** Y vs. La binary diagram showing no difference in the chemical composition between monazite crystals in the matrix and monazite included in garnet, **c** Chondrite-normalized REE patterns for monazite (Sun and McDonough 1989)

Inclusions in monazite

All types of monazite grains are generally free of cracks and display a large diversity of solid inclusions (Fig. 5a, S7, Tables S12 and S13), mainly concentrated in the core of the grains. Inclusions are elongated or sub-rounded, up to ~5 µm in

diameter. To obtain representative analyses of the inclusions, we carefully chose the inclusions occurring in a crack-free host, i.e., not displaying any connection with the matrix. Inclusions include rutile, chloritoid (X_{Fe} = 0.86–0.88), muscovite (Si = 3.31–3.43 p.f.u., X_{Na} = 0.04–0.09), paragonite (X_{Na} = 0.94) and zircon.

Monazite chemical composition

A large amount of monazite microanalyses (total number of analyses = 297) was performed on 112 monazite grains from the four thin sections (Fig. 5b). High-contrast BSE imaging and X-ray mapping show that monazite grains (both matrix and inclusion) in the two samples are nearly homogenous and have the same chemistry (Fig. S8). The chemistry of monazite (Table S14) reveals a significant brabantite substitution (Th^{4+} or $U^{4+} + Ca^{2+} = 2\ REE^{3+}$) accompanied by minor huttonite substitution (Th^{4+} or $U^{4+} + Si^{4+} = REE^{3+} + P^{5+}$) (Fig. S8). The Y content is always very low (< 0.8 wt%). The Th content varies from grain to grain (from 2 to 8.9 wt%), but no correlation between Th content and the textural position of the grain has been observed. Element X-ray maps for Th and chemical analyses also indicate that most of the monazite grains show a weak zonation in Th (Fig. S9), with an enriched core compared to the rim. Monazite grains display a high Sr concentration (700–1400 ppm) and a small Eu anomaly (Eu_N/Eu^*_N ~ 0.6). They are depleted in HREE at 10 times chondrite values (Fig. 5c; Tables S15 and S16).

We infer that the monazite and garnet rim grew under peak *P* conditions (~ 20 kbar), because monazite crystals are included in garnet rims, and both monazite inclusions and matrix grains contain HP inclusions. However, the textural equilibrium is not necessarily indicative of chemical equilibrium. To test the chemical equilibrium between monazite and garnet, partition coefficients for REE between neighbouring monazite and the low Y garnet rim ($^{REE}D_{mnz/g}$) have been calculated and represented in an array plot (Fig. 6a, as recently proposed by Taylor et al. 2017) and a traditional REE plot (Fig. S10). As no experimentally derived REE partitioning data exist for monazite, relationships have been determined by identifying trends based on our well-characterized natural examples. Garnet preferentially incorporates HREE ($0.2 < {}^{Yb}D_{mnz/g} < 2.1$), whereas monazite favours MREE, Sr, U and Th. $^{Y}D_{mnz/g}$ values range from 0.2 to 8.9. In the array plot (Fig. 6a), the monazite data form a distinct linear trend, suggesting chemical equilibrium of monazite with garnet rim.

Distribution, textural relationships and chemical composition of allanite

Allanite (total *n* = 39) occurs as inclusions in the garnet core (group 1) and in the matrix (group 2).

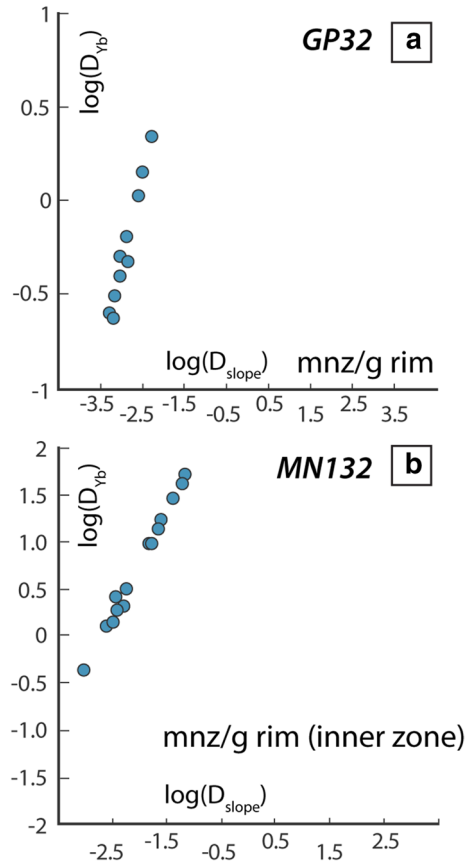

Fig. 6 Trace element partitioning calculated for **a** the monazite–garnet rim of the garnet–chloritoid micaschist (sample GP32, Gran Paradiso Unit) and **b** for the monazite–garnet rim (inner zone) of the garnet–albite micaschist (sample MN132, Money Unit). Data are plotted on array plots as recently proposed by Taylor et al. (2017). The partition coefficient of Yb between garnet and monazite (D_{Yb}) is plotted against the ratio D_{Yb}/D_{Gd} (D_{slope}). Data are plotted as log values. The array plot suggests a monazite equilibrium with a garnet rim in both samples

Allanite grains included in the garnet core (*n* = 14; ~25 to 50 µm in size) are elongated with sharp grain boundaries (Fig. 2d) or anhedral with indented grain boundaries. The anhedral grains frequently display BSE-bright rounded inclusions. A single grain displays a BSE-bright core surrounded by a BSE-dark rim, with a sharp boundary between the two domains (Fig. 7a). The difference in BSE brightness reflects the decrease in total REE from core to rim (Fig. 7a).

Matrix allanite crystals (25 to 200 µm in size) display irregular and indented grain boundaries and locally microinclusions (Fig. 7b). They form elongated fractured grains (*n* = 8), oriented parallel to the S_2 foliation, in chlorite or biotite aggregates. Together with apatite, they are also found (*n* = 10) in coronas around partially dissolved monazite crystals (groups 1.1. and 1.2).

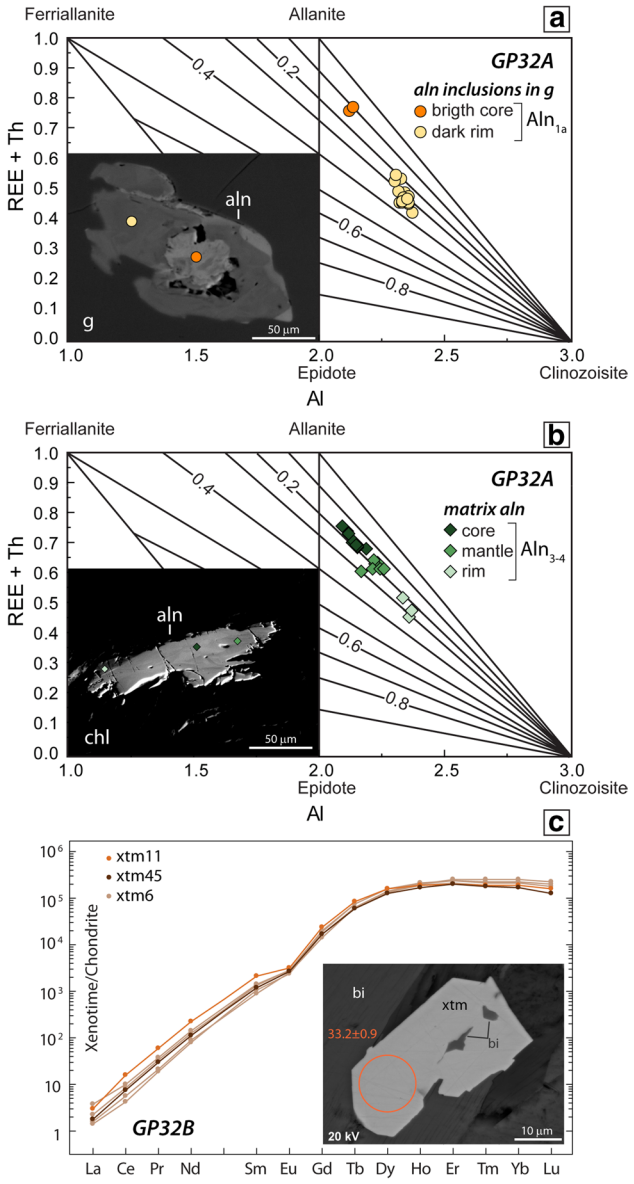

Fig. 7 Textural characteristics and chemical composition of allanite and xenotime from the Gran Paradiso Unit. **a, b** REE vs. Al (cation per formula unit) diagram showing the chemical zoning in the allanite–ferriallanite–epidote–clinozoisite system (Petrík et al. 1995) for allanite included in garnet (**a**) and matrix allanite (**b**). The colour-filled symbols (circle and diamond) indicate the location of the microprobe analyses, **c** Chondrite-normalized REE patterns for xenotime (Sun and McDonough 1989). The circle in the BSE image indicates the location of the LA-ICP-MS analysis and is ~12 µm in diameter; the number indicates $^{206}Pb/^{238}U$ age in Ma, with 2σ error

Anhedral allanite grains ($n = 7$), ~10 to 25 µm in size, rarely occur on chlorite or biotite aggregates that replace garnet porphyroblasts. Matrix allanite crystals show three concentric growth zones, with a decrease in total REE contents and BSE brightness from core to rim (Fig. 7b, Table S17).

Distribution, textural relationships and chemical composition of xenotime

Xenotime (total $n = 34$) is mainly found as anhedral grains, ~10 to 60 µm in size, in association with albite, chlorite (GP32A, GP32B) or biotite aggregates (GP32B) that replace garnet porphyroblasts (Fig. 2f). Xenotime is present instead of allanite when garnet is completely replaced by chlorite and biotite (Fig. 7c): it occurs in the cores as well as in the outermost domains of the previous garnet.

Chondrite-normalized REE patterns are similar for all xenotime grains (Fig. 7c), with HREE enrichment, a small Eu anomaly and with relatively high Th/U (0.04–0.26; Table S18). The Sr concentration is low (18–22 ppm). The LREE contents are low and fall within the range of a few tenths of a weight percent. The Thorium (27–580 ppm) and U concentrations (650–4956 ppm) are variable.

U–Th–Pb results

Irrespective of the textural position of the monazite (in the matrix or included in garnet), $^{208}Pb/^{232}Th$ ages range between 39.3 ± 1.0 and 46.4 ± 1.2 Ma (Fig. 8a, b), with a $^{208}Pb/^{232}Th$ weighted average age at 41.5 ± 0.3 Ma ($n = 34$; MSWD = 3.4). Monazite grains containing HP inclusions (rutile, chloritoid, high-Si muscovite and paragonite) yield a $^{208}Pb/^{232}Th$ weighted average age at 41.2 ± 0.5 Ma ($n = 11$; MSWD = 1.9).

U–Th/Pb ratios from matrix allanite crystals were measured in the same sample. All analyses show a large and variable amount of common Pb (Table S6). The free regression line of 26 analyses in the Tera–Wasserburg (total Pb) diagram defines an initial $^{207}Pb/^{206}Pb$ composition of 0.842 ± 0.0012 and a lower intercept age of 32.7 ± 4.2 Ma (MSWD = 0.4, $n = 26$; Fig. 8d). The initial $^{207}Pb/^{206}Pb$ is in agreement with the model Pb composition at 33 Ma (~0.838 ± 0.015, Stacey and Kramers 1975).

Twenty-seven spots on 17 xenotime grains from sample GP32 are reported in a Tera–Wasserburg diagram (Fig. 8d). Most of them show common Pb contamination. The $^{206}Pb/^{238}U$ ages of the concordant data range from 30.4 ± 0.8 to 34.4 ± 0.8 Ma, with a single spot at 38.5 ± 1.3 Ma in a xenotime inclusion in a matrix biotite (which was not considered further). The $^{206}Pb/^{238}U$ weighted average age is at 32.3 ± 1.0 Ma ($n = 11$; MSWD = 8.2; Table S7, Fig. 8d).

Results for the Money Unit

Petrography (sample MN132)

The two studied thin sections of sample MN132 are cut perpendicular to the foliation, one parallel (MN132A) and the

other perpendicular (MN132B) to the stretching lineation. Sample MN132 consists of quartz, white mica, garnet, chlorite, albite, and accessory chloritoid, rutile, ilmenite, monazite, apatite and zircon. Table S9b summarizes the deformation/mineral growth relationships of this sample. Inclusions in garnet porphyroblasts (see the following paragraph for a detailed description) and microlithons with relicts of an earlier microfolded schistosity are ascribed to stage 1 (Fig. S11a). The S_1 foliation is marked by the shape-preferred orientation of muscovite, paragonite and by elongated crystals of rutile. The dominant foliation S_2 (stage 2) is marked by the shape-preferred orientation of white mica, chlorite, ilmenite and by discontinuous quartz layers (Fig. S11b). Chlorite forms flattened aggregates, 0.5–2 mm long (X_{Fe} = 0.58–0.62; X_{Mn} < 0.01; $X_{Al,T2}$ = 0.63–0.64). Aggregates of chlorite (X_{Fe} = 0.61–0.66; X_{Mn} < 0.01; $X_{Al,T2}$ = 0.66–0.71) as well as locally biotite also in places partly replace garnet porphyroblasts (stage 3).

Garnet

In sample MN132, garnet occurs as polygonal or rounded porphyroblasts (< 2 mm), wrapped by the S_2 foliation (Fig. S11b). Garnet has an inclusion-rich inner zone, from 100 µm to ~ 1 mm in diameter (garnet 1) and a thin outer zone (< 150 µm, garnet 2; Fig. 9). The latter is generally inclusion free, with the exception of some rare tiny monazites (~ 10 to 30 µm) and larger apatite crystals (< 50 µm).

Garnet 1 contains numerous inclusions of quartz, chloritoid (X_{Fe} = 0.88–0.90), ilmenite (commonly replaced by rutile), apatite, monazite and zircon (Fig. 9a, c, Table S19). Chloritoid has not been identified in the matrix, suggesting that it was present as a matrix phase prior to garnet growth and reacted out during the initial garnet formation.

Garnet is almandine-rich (alm_{64-85}, gr_{4-11}, py_{3-6}, $spss_{4-16}$) and displays concentric zoning of Fe, Mn and Mg, and an irregular sector zoning for Ca (Fig. 9a, b, S12, Table S20). Spessartine displays a bell-shaped decrease (16–4 mol%) from core to rim, balanced by an increase in almandine (64–85 mol%) and pyrope contents (3.8–5.5 mol%). The zoning pattern for the pyrope content is nevertheless characterized by a hexagonal band of high Mg concentration ($py_{4.9}$) that marks the boundary between garnet zones 1 and 2. In garnet 1, Ca displays both sector zoning and patchy zoning. Elongated domains with low-Ca content (gr_{4-5}, Fig. 9a) are dispersed in garnet 1, where they locally form coronas around chloritoid inclusions. Such a domain in garnet 1 may result from the partial dissolution of chloritoid (or chlorite) inclusions, and their replacement by low-Ca garnet. The HREE and Y contents decrease from core to rim (Dy_N/Yb_N = 0.54, 2.0–11.9 and 3.9–18.8 in garnet 1a, 1b–c and garnet 2, respectively), whereas the MREE slightly increase (Dy_N/Gd_N = 10.5, 0.7–4.0, and 0.9–2.2 in garnet 1a, 1b–c and garnet 2, respectively; Fig. 9d, S12, Table S21).

White mica

White mica occurs (1) as inclusions (20–200 µm) of either paragonite (X_{Na} = 0.83–0.95) or muscovite (3.33 < Si < 3.47 p.f.u., X_{Na} = 0.04–0.07; Fig. S13, Table S22) in albite (Fig. S11c), (2) in the matrix as large muscovite flakes (300–500 µm) overgrowing S_2 (Fig. S11d), displaying decreasing Si content and increasing X_{Na} and X_{Fe} from core (Si = 3.26–3.51 p.f.u.; X_{Na} = 0.03–0.08; X_{Fe} = 0.40–0.54, Table S8) to rim (Si = 3.08–3.35 p.f.u.; X_{Na} = 0.06–0.17; X_{Fe} = 0.46–0.56, Table S22), and (3) in the matrix oriented parallel to the S_1 and S_2 foliations (30–200 µm). Muscovite defining S_1 and S_2 shows chemical zoning, with decreasing Si content and increasing X_{Na} and X_{Fe} from core (Si = 3.31–3.48 p.f.u.; X_{Na} = 0.02–0.08; X_{Fe} = 0.38–0.54) to rim (Si = 3.10–3.29 p.f.u.; X_{Na} = 0.07–0.19; X_{Fe} = 0.48–0.58) (Fig. S13, Table S22).

P–T results

The *P–T* evolution of sample MN132 was modelled using the system composition SC4 (Table S2), obtained by XRF analysis of the rock chip from which the thin section was cut. No attempt has been made to remove the garnet cores from this bulk composition. This choice results from the fact that sample MN132 displays a low modal amount of garnet and inclusion-rich cores. Previous studies on similar pelitic rocks (e.g., López-Carmona et al. 2013) have shown that these effects are negligible, especially if the modal amount of garnet is low, as in the studied sample. In addition, removing the inclusion-rich garnet cores would result in (1) a new bulk composition barely different from the initial one if the inclusion association approaches that of the matrix at that moment of the *P–T* evolution; or (2) a new bulk composition associated with additional uncertainty related to the problematic estimation of the amount and composition of the inclusions to be removed. Therefore, the effects of modifying the bulk composition in terms of removing the garnet core have been checked by varying the analysed values of Ca, Al, as well as the proportion of Fe^{3+}. The results indicate that these effects are negligible in the case of sample MN132.

The earlier history of sample MN132 (stage 1) is characterized by the relict garnet–chloritoid–rutile–paragonite–glaucophane assemblage, with paragonite and glaucophane observed as inclusions in albite and monazite, respectively. In the calculated pseudosection for sample MN132 (Fig. 10), the corresponding stability fields occur at T < 550 °C, P > 14 kbar, in line with previous estimates for peak *P–T* conditions in sample MN2 (Manzotti et al. 2015b). The absence of chloritoid in the matrix suggests

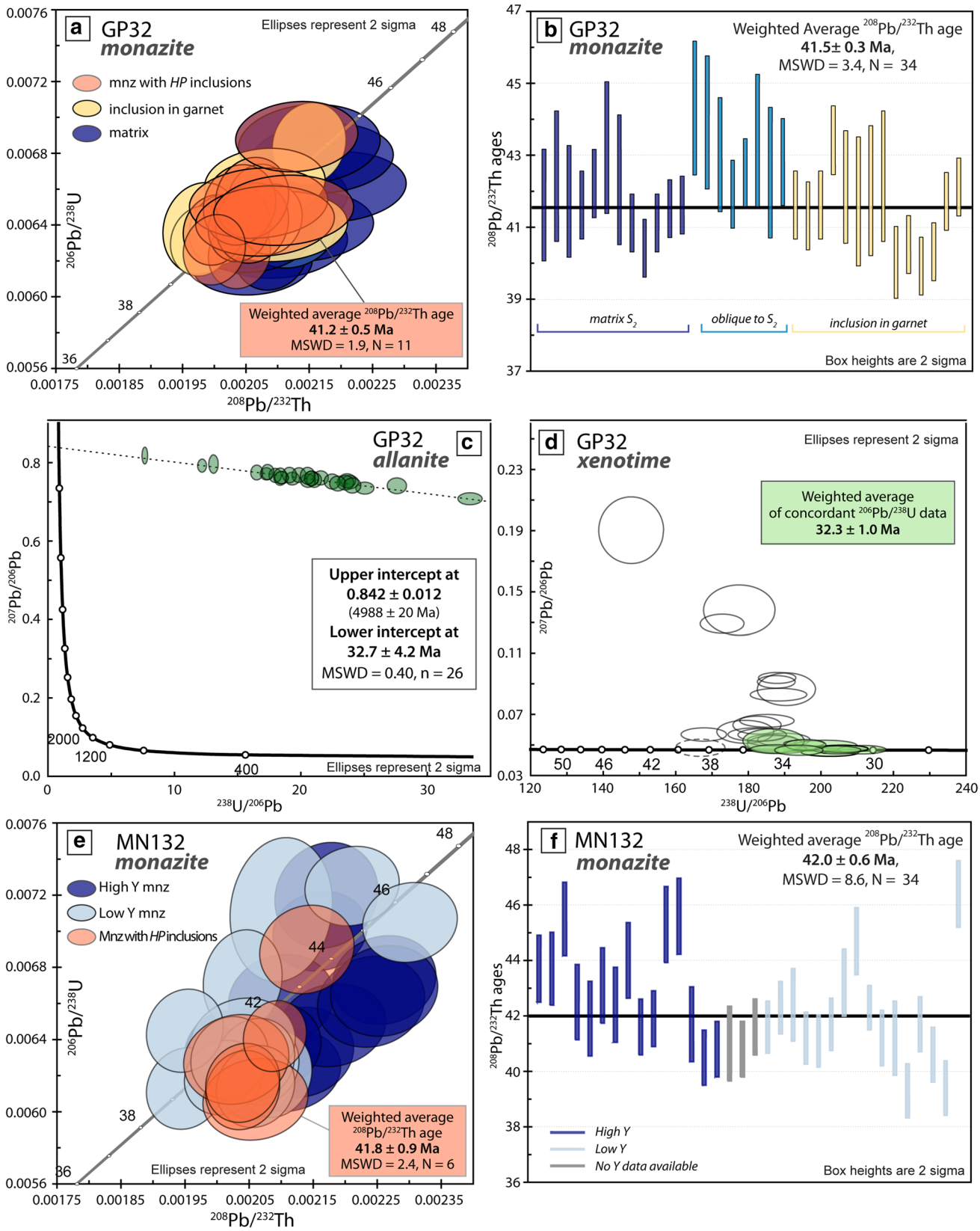
a GP32 monazite
Ellipses represent 2 sigma
mnz with HP inclusions
inclusion in garnet
matrix
Weighted average 208Pb/232Th age
41.2 ± 0.5 Ma
MSWD = 1.9, N = 11
206Pb/238U
208Pb/232Th
b GP32 monazite
Weighted Average 208Pb/232Th age
41.5± 0.3 Ma,
MSWD = 3.4, N = 34
208Pb/232Th ages
matrix S2
oblique to S2
inclusion in garnet
Box heights are 2 sigma
c GP32 allanite
Upper intercept at
0.842 ± 0.012
(4988 ± 20 Ma)
Lower intercept at
32.7 ± 4.2 Ma
MSWD = 0.40, n = 26
Ellipses represent 2 sigma
207Pb/206Pb
238U/206Pb
d GP32 xenotime
Ellipses represent 2 sigma
Weighted average
of concordant 206Pb/238U data
32.3 ± 1.0 Ma
e MN132 monazite
High Y mnz
Low Y mnz
Mnz with HP inclusions
Weighted average
208Pb/232Th age
41.8 ± 0.9 Ma
MSWD = 2.4, N = 6
Ellipses represent 2 sigma
f MN132 monazite
Weighted average 208Pb/232Th age
42.0 ± 0.6 Ma,
MSWD = 8.6, N = 34
High Y
Low Y
No Y data available
Box heights are 2 sigma

◂**Fig. 8** Age results for the Gran Paradiso and Money Units. All data are uncorrected for common Pb. **a** $^{206}Pb/^{238}U$ vs. $^{208}Pb/^{232}Th$ diagram for the Gran Paradiso monazite (sample GP32). **b** Weighted average Th–Pb age for the Gran Paradiso monazite (sample GP32). **c** Tera–Wasserburg diagram of a free regression of uncorrected U–Pb allanite data. The initial Pb composition is similar to a model of Pb composition at 33 Ma (0.838 ± 0.015, Stacey and Kramers 1975). **d** Xenotime U–Pb data plotted in a Tera–Wasserburg plot for the GP32 sample (Gran Paradiso Unit). **e** $^{206}Pb/^{238}U$ vs. $^{208}Pb/^{232}Th$ diagram for the Money monazite (sample MN132). **f** Weighted average Th–Pb age for the Money monazite (sample MN132)

equilibration in the stability fields of either garnet–glaucophane–paragonite–rutile (indicating increasing *T*) or garnet–glaucophane–chlorite–paragonite–rutile (indicating decreasing *P*).

The complex textural record and chemical zoning in this garnet require a detailed analysis to constrain the trajectory of the *P–T* path. The chemical zoning is characterized by a continuous rimward decrease of spessartine in garnet 1 (1a to 1c, Fig. 9), followed by a very narrow plateau or a slight increase at the transition from garnet 1 to garnet 2, then a slight decrease in garnet 2, followed locally by a slight increase in the outermost rim. Grossular is variable (in the range of a few mole percent), but is roughly constant in garnet 1, then strongly decreases in garnet 2. Spessartine isopleths have steep slopes (nearly isothermal) in all mineral assemblages, whereas the isopleths for grossular display a drastic change when crossing the lawsonite-out reaction (Fig. 10a). Consequently, the decrease in spessartine reflects garnet 1 growth during increasing *T*, whereas the lack of significant grossular variation would imply increasing *P* (a *P–T* evolution following the grossular isopleths). A straightforward explanation for the Ca and Mn distribution across the garnet from sample MN 132 would be, therefore, to consider that the transition from garnet 1 to garnet 2 records the disappearance of lawsonite from the mineral assemblage at equilibrium with the growing garnet. However, the analysed content of grossular does not match the values calculated in the pseudosection. Potential explanations for this discrepancy may be (1) uncertainties in thermodynamic modelling (thermodynamic parameters for end-members, solid solution models, etc.), or (2) the failure of the kinetic factors responsible for Ca to achieve chemical equilibrium during garnet growth, or (3) problems related to accurately establishing the effective equilibration volume and hence the bulk composition. Due to these difficulties, it is probably premature to interpret the small, but consistent, variations in the garnet chemistry as being indicative of a more complex *P–T* path than a simple loop as drawn in Fig. 10.

To overcome these difficulties in matching measured and calculated compositions of minerals in the pseudosection, additional constraints on the trajectory of the *P–T* path and the peak conditions reached have been obtained by other approaches. Garnet–chloritoid thermometry (Perchuk 1991), applied to the garnet 1 and chloritoid inclusions, yields a temperature of 541 ± 19 °C. A maximum temperature of 542 ± 29 °C was estimated using the RSCM method of Beyssac et al. (2002, 2003). As this *T* estimate is pressure independent, the peak *T* may be reached either at peak *P* or during decompression. However, these *T* ranges are consistent with those of the peak assemblages calculated in the phase diagram (Fig. 10).

P constraints were obtained using the recently developed barometers based on the elastic properties of quartz inclusions and their garnet host (Guiraud and Powell 2006; Kohn 2014). Details about the method are given in the ESM. Taking into account the potential caveats of this method, we collected 66 Raman spectra on 49 quartz grains included in 12 garnet crystals (Fig. S14, Tables S23 and S24). The results show negligible or low residual pressures in a large number of quartz inclusions, including the largest grains (> 50 µm). These results can be explained by the numerous fractures observed in the large quartz grains. By contrast, the rounded, fracture-free quartz inclusions that do not exceed 5 µm provide the largest residual pressures. Using the calibration of Ashley et al. (2014), the Qui*B* barometry of quartz inclusions yields a minimum entrapment *P* of 16.9 and 17.7 kbar (± 1 kbar) at a nominal *T* of 500 and 550 °C, respectively. These values are consistent with the stability field of the assemblage in equilibrium with garnet 1 (glaucophane–chloritoid–paragonite–rutile; Fig. 6). Therefore, we infer peak *P–T* conditions of ~ 17 to 18 kbar and 520–550 °C for stage 1. These new values are consistent with the previous calculations for the Money Unit (Manzotti et al. 2015b), but they refine the uncertainty on the peak *P*.

The observed assemblage garnet–chlorite–ilmenite (stage 2, S_2) is stable in the range ~ 480–560 °C, at a maximum *P* of 14 kbar. The *T* range overlaps the range independently estimated using the RSCM method. The corresponding fields contain paragonite and glaucophane at higher *P* (from 10 to 14 kbar) and albite at lower *P*. However, these indications should only be used for qualitative purposes, since the development of the chlorite pseudomorphs, albite and ilmenite replacing rutile are not necessarily contemporaneous. Furthermore, they are governed by local equilibria, for which the pseudosection, calculated for the bulk-rock composition, is not necessarily strictly appropriate.

Textural characteristics and chemical composition of the accessory phases

Monazite grains identified in both thin sections do not have an allanite rim. Xenotime has never been observed.

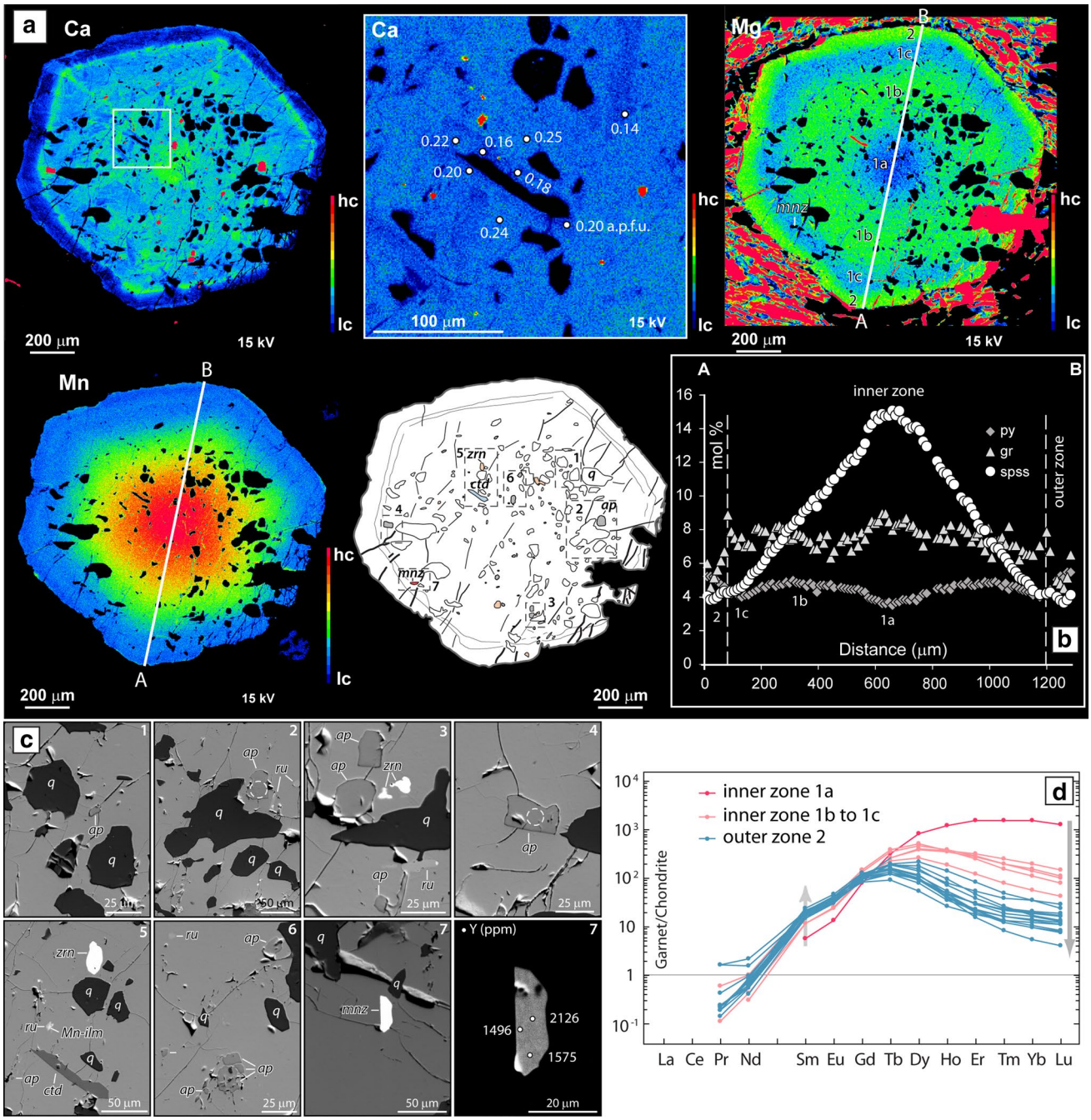

Fig. 9 Garnet chemistry from sample MN132 from the Money Unit. **a** X-ray mapping images and drawing of a garnet porphyroblast (*hc* high concentration; *lc* low concentration). **b** Compositional profile of garnet along the white line A–B traced in **a**, displaying the different growth zones (1a, 1b, 1c and 2). **c** BSE images of the major and accessory phases included in garnet 1. Major: quartz and chloritoid. Accessory: ilmenite, rutile, apatite, zircon and monazite. Monazite is found in garnet 1c. Analysed spots for REE on apatite are indicated by dashed white circles (diameter: 12 µm). **d** Garnet REE plot, normalized to chondrite values provided by Sun and McDonough (1989)

Monazite distribution and textural relationships

In sample MN132, monazite (total $n = 152$) occurs as inclusions in garnet and ilmenite (group 1) and in the matrix (group 2) (Table S12). Monazite inclusions in garnet ($n = 24$) are generally smaller (~ 10 to 30 µm in size) than those in the matrix. They occur as euhedral (locally mimicking a cube), sub-rounded or elongated crystals, mainly in the outermost domains of garnet porphyroblasts (rim of growth zone 1 or in growth zone 2), characterized by a slight decrease in grossular (Fig. 9). In garnet partially replaced by chlorite at the rim, monazite crystals display internal straight and

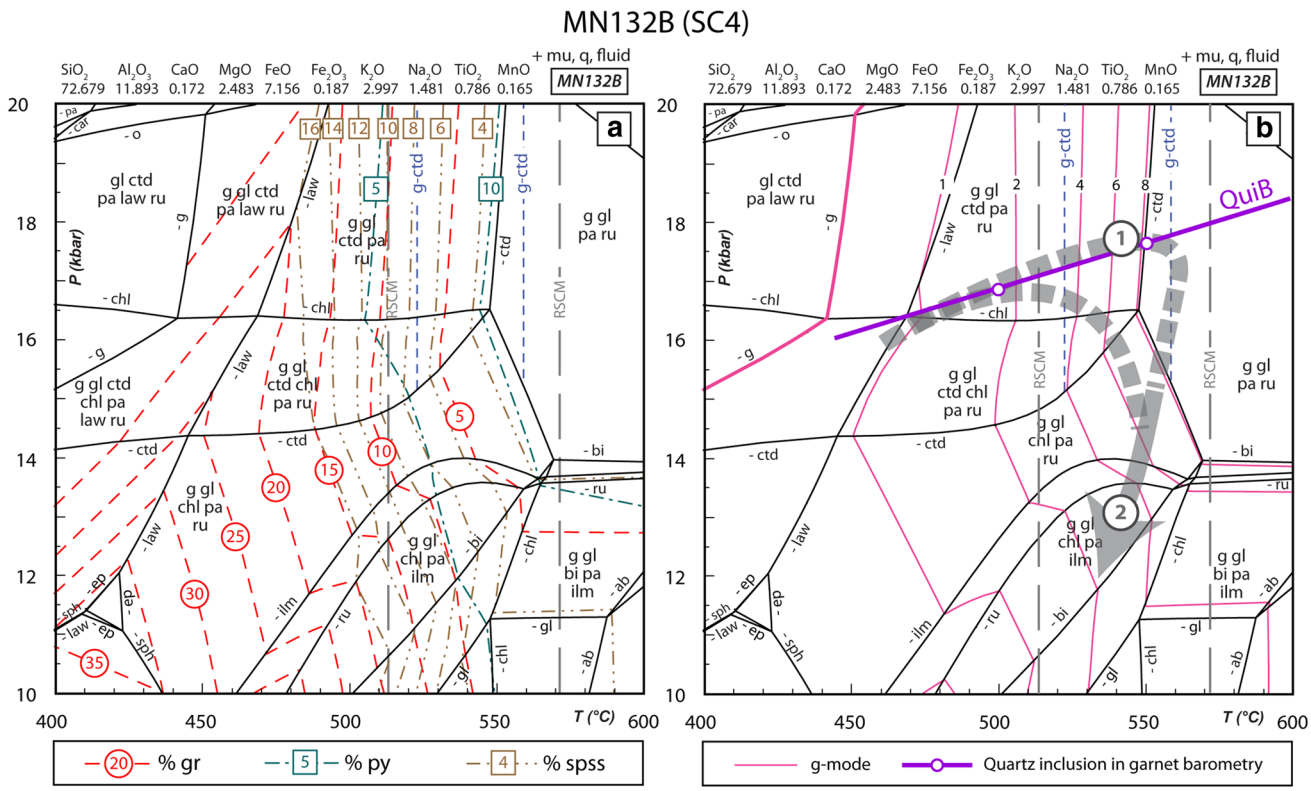

Fig. 10 *P–T* pseudosections, calculated for the garnet–albite-bearing micaschist (sample MN132, Money Unit). Compositional isopleths for garnet (X_{Ca}, X_{Mn}, X_{Mg}), RSCM (grey fine dashed lines), garnet–chloritoid thermometry (blue fine dashed lines) and Qui*B* barometry (green line) results are also shown. The grey arrow indicates the inferred *P–T* path

well-defined boundaries with garnet and external irregular and resorbed grain boundaries with chlorite. A single, prismatic elongated monazite inclusion with straight grain boundaries (~ 20 µm) has been found in ilmenite. Matrix monazite grains (group 2; $n = 121$) do not show any preferred orientation with respect to the S_1 or S_2 foliations. Crystals are mainly stubby with sub-rounded contours or locally elongated (~ 20 to 50 µm in length). Monazite is associated with muscovite, quartz bands and rarely chlorite. Few grains are in contact with ilmenite or associated with albite ($n = 6$).

Inclusions in monazite

All types of monazite grains contain a variety of monomineralic inclusions, up to 2–3 different types per grain. Inclusions are rounded or slightly elongate, ~ 5 µm in diameter. They occur in matrix grains (mainly at the rim) and in monazite included in garnet that do not show the Y-rich core (see paragraph below). To ensure that inclusions are representative of stable matrix phases during monazite growth, we selected grains that are included in a crack-free host. We were also careful to select only inclusions without any connection with the matrix, any secondary products between their rim and the host mineral. Inclusions (Fig. 11a, S15, Table S25) comprise quartz, rutile, garnet, chloritoid ($X_{Fe} = 0.89$), paragonite ($X_{Na} = 0.89$–0.93), muscovite (Si = 3.33–3.40 p.f.u., $X_{Na} = 0.07$–0.08) and ferroglaucophane (according to the classification of Leake et al. 1997) (Si = 7.91 p.f.u., $X_{Na} = 0.97$, $X_{Fe^{2+}} = 0.57$, $X_{Fe^{3+}} = 0.06$).

Monazite chemical composition

The composition of monazite is dominated by brabantite substitution with an influence of huttonite substitution (Table S26, Fig. S16). Most of the grains display a consistent and distinctive Y zonation with a decreasing concentration from core to rim with a variation of up to one order of magnitude. A weaker zonation of the same type is also observed for U (Fig. 11b, c). Matrix monazite generally shows two chemically distinct growth zones, clearly visible on the Y and U maps and separated by a sharp boundary. The La and Ce concentrations generally decrease rimward, whereas Gd slightly increases. The first growth zone contains the highest HREE ($Dy_N/Yb_N = 40$–60) and Y concentrations (Y ~ 4500 to 17,100 ppm) and it is found as distinct innermost cores or rarely as whole grains (Fig. 11c, d). The second growth zone commonly occurs as a mantle domain surrounding the first

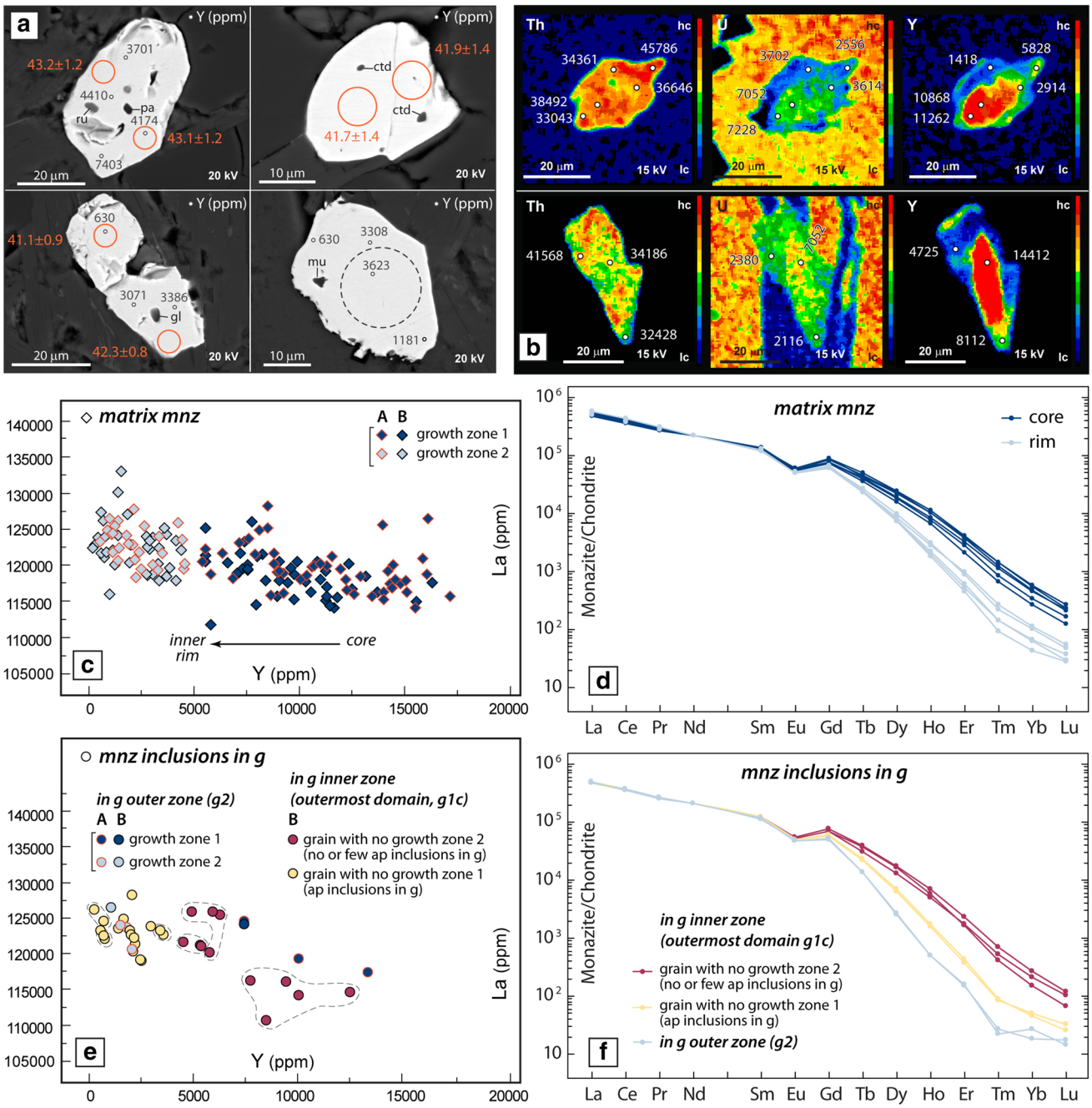

Fig. 11 Chemical composition of monazite from the Money Unit. **a** BSE images of matrix monazite. Monazite grains display inclusions of rutile, paragonite, chloritoid, glaucophane and Si-rich muscovite. Analysed spots are indicated by orange circles (diameter: 7 and 9 µm) for isotopic dating and by dashed grey circles (diameter: 15 µm) for REE. The numbers indicate the $^{208}Pb/^{232}Th$ ages in Ma with 2 σ error. The small white filled circles indicate the location of the microprobe analyses, for which the Y content is reported in ppm. **b** X-ray mapping images of monazite grains (*hc* high concentration; *lc* low concentration). The apparent high U concentration of the mineral surrounding monazite (i.e. white mica) is due to an interference between the U and K peaks of the β line, measured on the PET spectrometer (U ~ 0.42776, K ~ 0.424). The small white filled circles indicate the location of the microprobe analyses, for which the Y content is reported in ppm. **c** Y vs. La binary diagram for matrix monazite, showing two distinct growth zones: an Y-rich core and a Y-poor rim. **d** Chondrite-normalized REE patterns for matrix monazite (Sun and McDonough 1989). **e** Y vs. La binary diagram for monazite included in garnet. The chemical zoning between growth zones 1 and 2 is only observed in a few grains. Monazite included in garnet with several apatite inclusions displays low Y content. **f** Chondrite-normalized REE patterns for matrix monazite (Sun and McDonough 1989)

growth zone. It displays low Y concentrations (< 4500 ppm) and a decrease in the HREE concentration (Dy_N/Yb_N = 70–160), Fig. 11d. Rarely, the second growth zone forms whole grains that are always characterized by high-*P* inclusions (i.e., rutile, paragonite, glaucophane and muscovite, Fig. 11a).

Monazite grains included in garnet may be classified in three main groups, based on their core-rim relationships, their Y concentration, their position within the garnet and the presence or absence of apatite inclusions. The first group comprises few monazite grains showing the two chemical growth zones, with a Y-rich core and a Y-poor rim (Fig. 11e, Table S26). These grains are found in the garnet outer zone (growth zone 2) and are characterized by low HREE. The second group comprises monazite grains without a Y-poor rim that are mainly located in the outermost domain of garnet inner zone 1; the latter displays either no or rare apatite inclusions (Fig. 11e, f, Table S27). This group shows relatively high HREE. The third group comprises monazite grains without a Y-rich core: these grains occur at the outermost domain of garnet growth zone 1 and in garnets characterized by abundant apatite inclusions (Figs. 9, 11e, f, Table S27). They display relatively low HREE (Fig. 11f). All monazite grains (i.e., in the matrix and included in the garnet) show a high Sr concentration (800–2200 ppm, Table S27).

Partition coefficients for REE between neighbouring monazite and garnet ($^{REE}D_{mnz/g\ rim\ inner\ zone}$) were calculated (Fig. 6b, S17a) to test their chemical equilibrium. Due to their small size, the few monazite crystals located in garnet 2 (Fig. 9) could not be analysed. Therefore, only monazite crystals in the outermost domain of garnet 1 (i.e., zone 1c, Fig. 9) were analysed. The high or low Y content of these monazite crystals is related to the absence or presence of apatite inclusions in garnet, respectively (see the "Monazite chemical composition" section and Fig. 11 for more details). Monazite data form a distinct linear trend in the array plot, suggesting chemical equilibrium with the rim (zone 1c) of garnet 1 (Fig. 9).

Distribution, textural relationships and chemical composition of apatite

Apatite is abundant as inclusions in garnet (< 50 µm) and in the matrix. Apatite grains included in garnet display different shapes, from rounded to polygonal. In the few cases where apatite and monazite are in contact, then the grain boundaries are interlobate. In the matrix, two types of apatite have been observed: large (> 200 µm) slightly elongate crystals (apatite-I) and small (< 100 µm) sub-rounded grains (apatite-II). Apatite-I and apatite included in garnet show a similar REE pattern (Fig. S18a. Tables S28–29), with high Y concentrations (up to 2000 ppm) and a decrease in HREE from core to rim (Dy_N/Yb_N core = 1.5–3.1, Dy_N/Yb_N rim = 3.6–6.3; Dy_N/Yb_N inclusion in garnet = 2.9–4.4). The Eu anomaly is locally strong in the apatite-I core (Eu_N/Eu^*_N = 0.3). MREE slightly increase in the apatite-I rim (Dy_N/Gd_N core = 0.7–1.0, Dy_N/Gd_N rim = 0.5–0.9). Therefore, both apatite inclusions and apatite-I in the matrix are hereafter referred to as apatite-I. Apatite-II shows a weak Eu anomaly (Fig. S18b, Tables S28–29), as observed in the rim of apatite-I (Eu_N/Eu^*_N = 0.6–0.7), and a strong depletion in HREE (Dy_N/Yb_N = 8–25) with low Y content.

The chemical equilibrium between matrix monazite and apatite-I as well as between apatite-I and garnet was tested by calculating their partition coefficients for REE between neighbouring grains. The two diagrams (Figs. S17b, c) show a weakly defined array with some dispersed points, suggesting no chemical equilibrium between matrix monazite and apatite-I and apatite-I and garnet. By contrast, matrix monazite (core and rim) and apatite-II, and apatite-II and the garnet outer zone (i.e., garnet 2) form linear trends, suggesting that they were in chemical equilibrium during their growth (Figs. S19a, b).

U–Th–Pb results

In the Money sample (MN132), only monazite was dated (Table S8). The ^{208}Pb–^{232}Th ages (corresponding to less than 20% of common Pb) are scattered between 39.3 ± 1.0 and 46.4 ± 1.2 Ma, allowing to calculate a weighted average age of 42.0 ± 0.6 (MSWD = 8.6; *n* = 34; Fig. 8e, f and Table S8). The high Y matrix monazite cores yield a weighted average $^{208}Pb/^{232}Th$ age of 42.7 ± 0.9 Ma (*n* = 13, MSWD = 5.5), which is marginally older than the low Y monazite rims (weighted average $^{208}Pb/^{232}Th$ age at 41.7 ± 0.9, *n* = 16, MSWD = 10). Monazite grains containing HP inclusions (glaucophane, paragonite, rutile, chloritoid, high-Si muscovite; Table S8) yield a $^{208}Pb/^{232}Th$ weighted average age of 41.8 ± 0.9 Ma (*n* = 6; MSWD = 2.4).

Discussion

Linking metamorphic parageneses with the growth/dissolution of accessory phases

Several approaches have been used to constrain the relative timing of the growth of accessory and major mineral phases and to link the growth of these minerals with the *P–T* evolution of the studied samples. For instance, textural relationships (e.g., coronas) have been examined to determine the chemical reactions responsible for the growth or dissolution of accessory phases (e.g., Spear and Pyle 2002; Grand'Homme et al. 2016). Mineral inclusions require careful discussion, because they can be unreactive phases sealed

within a growing mineral (e.g., detrital zircon in a growing garnet) or phases that are chemically equilibrated with their host during its growth (e.g., Regis et al. 2016). Trace element signatures of major and accessory phases were used to assess their relative timing of growth, whereas the partition coefficients for REE were calculated to test their chemical equilibrium.

Gran Paradiso Unit

In the Gran Paradiso sample (GP32), garnet is zoned in major and trace elements. Thermodynamic modelling indicates that the high Y garnet core crystallized at ~ 18 to 20 kbar, ~ 480 to 520 °C (stage 1a) (Fig. 12), whereas the low Y garnet rim grew under peak conditions at ~ 20 kbar, ~ 520 to 540 °C (stage 1b) (Manzotti et al. 2015b). The garnet was still stable and its modal proportion did not change during decompression between stages 1b (~ 20 kbar) and 2 (~ 12.5 to 14.5 kbar) (Fig. 3a). Inclusions in garnet comprise a first generation of allanite in the high Y garnet core, whereas monazite occurs in the low Y garnet rim. The first generation of allanite is absent in the matrix, suggesting that it became unstable during garnet growth (e.g., Smith and Barreiro 1990; Fitzsimons et al. 2005; Spear 2010). The reaction responsible for monazite formation most likely involved the dissolution of allanite and required a source of phosphorous, such as apatite or xenotime.

HP mineral inclusions, such as rutile, chloritoid, Si-rich muscovite and paragonite, are present in monazite included in garnet as well as in monazite in the matrix. Matrix monazite grains are generally oriented parallel to the main foliation S_2, the regional fabric developed during the thrusting of the Gran Paradiso Unit on top of the Money Unit at ~ 12.5 to 14.5 kbar, ~ 530 to 560 °C. However, some corroded grains are oriented at a high angle with respect to the main fabric. Regardless of their relationships with the superposed fabrics, all monazite grains are chemically homogeneous and characterized by a low Y content, a slightly negative Eu anomaly and a steep negative HREE pattern. Monazite–garnet rim trace element partitioning indicates that the monazite and garnet rim grew together in equilibrium. In addition, matrix monazite and monazite included in garnet yield a single age cluster at 41.5 ± 0.3 Ma. Selecting only monazite with HP inclusions, a weighted average age of 41.2 ± 0.5 Ma is obtained. Therefore, on the basis of all these observations, we infer that monazite, both in the matrix and included in garnet, crystallized close to peak *P* conditions (at ~ 20 kbar, ~ 520 to 540 °C, i.e., during the growth of the garnet rim) and that most of the matrix monazite grains were subsequently re-oriented parallel to the main regional S_2 foliation.

A second generation of allanite is observed (1) as single crystals in a chlorite matrix, frequently in strain shadows of dissolving garnet porphyroblasts (Fig. 7b) and (2) as aggregates of small crystals together with apatite, forming coronas around monazite. The second occurrence is mainly found on muscovite aggregates defining the main S_2 foliation. HP mineral inclusions (e.g., paragonite or chloritoid, see Fig. 3a for their stability fields) have never been observed in the second generation of allanite. Textural relationships suggest that the growth of allanite-II may be related to the dissolution of monazite and the contemporaneous crystallization of

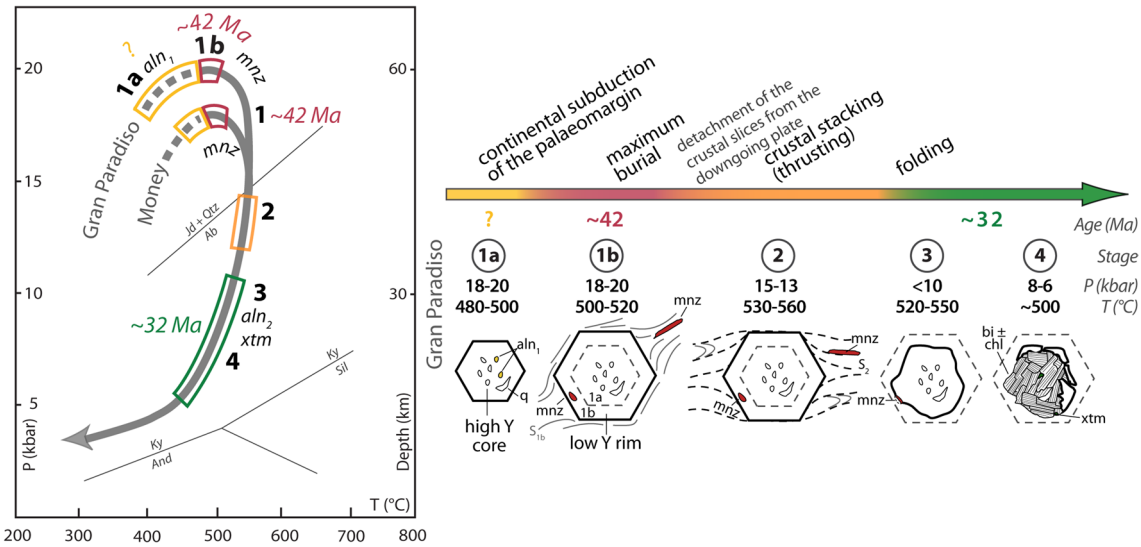

Fig. 12 Summary of the petrochronological results (*P–T* paths and monazite, allanite and xenotime ages) for the Gran Paradiso and Money Units. Interpretative sketches for the Gran Paradiso sample show the growth of accessory and major phases combined with *P–T* conditions and ages (*t*)

new apatite. Its growth occurred during garnet consumption at *P* lower than ~9 to 10 kbar during stages 3 and 4 (Fig. 3d) at 32.7 ± 4.2 Ma.

Xenotime is almost only found in association with biotite ± chlorite aggregates replacing garnet porphyroblasts (in the type-II domain, sample GP32B). Consumption of garnet (e.g., Pyle and Spear 1999) and dissolution of monazite and/or apatite may, therefore, result in the growth of xenotime during stages 3 and 4, with garnet representing the principal yttrium source (Fig. 12). *P*–*T* modelling (at H_2O-undersaturated conditions, Fig. 4b) suggests that the breakdown of garnet occurred at ~9 to 10 kbar and ~500 to 550 °C and that the amount of biotite increased with decreasing *P*. Xenotime yields a weighted average U–Pb age of 32.3 ± 1.0 Ma.

Money Unit

In the Money sample, garnet displays a typical Mn zoning characterized by a gradual decrease in Mn content from core to rim, suggesting a temperature increase during garnet growth. The patchy and sector zoning observed for Ca in the inner garnet zone (garnet 1) contrasts with the concentric zoning patterns of Fe, Mn and Mg, and likely results from local Ca release after reactions involving calcic phases, such as plagioclase, epidote, lawsonite, or apatite. The inner garnet zone contains numerous inclusions of quartz and apatite and minor inclusions of chloritoid, ilmenite breaking down to rutile, monazite and zircon. The outer garnet zone is generally inclusion free, with the exception of very rare monazite. The small number of inclusions in the garnet rim with respect to the core likely reflects a decrease in the growth rates (e.g., Yang and Rivers 2001).

The high concentration of HREE and Y in the inner garnet zone results from the dissolution of a REE- and Y-rich phase (i.e., apatite, xenotime and/or monazite). Similarly, the breakdown of apatite-I during garnet growth can explain the slight increase in MREE (e.g., Sm) observed in garnet (Fig. 9d), as reported in other case studies (e.g., Regis et al. 2014b). Trace element partitioning between apatite-I and garnet suggests that they were not in chemical equilibrium (Figs. S17e, f). We, therefore, infer that apatite-I was partially dissolved during garnet growth. The dissolution of apatite-I provides MREE, Y and P, thereby allowing the development and growth of monazite grains. The variation in Y concentrations in monazite included in garnet is probably controlled by the dissolution of apatite that supplies Y to the system during monazite growth. In the matrix, the monazite core displays high Y concentrations, a slightly negative Eu anomaly and a steep HREE pattern. The monazite rim shows low Y concentrations, a slightly negative Eu anomaly and a decrease in HREE. Inclusions of HP minerals (such as chloritoid, glaucophane and paragonite) are mainly found in the low Y rim. Trace element partitioning between monazite and apatite-I indicates chemical disequilibrium. By contrast, partition coefficients for REE between monazite and the outermost domain of garnet 1 (zone 1c, Fig. 9) suggest that they grew together in equilibrium.

Therefore, these observations suggest that the breakdown of Y-rich apatite-I triggers the crystallization of Y-rich monazite with coeval garnet (inner zone) during the prograde to peak evolution (~17 to 18 kbar and ~550 °C) at 42.0 ± 0.6 Ma. A weighted average of 41.8 ± 0.9 Ma has been obtained when selecting monazite with HP inclusions.

Timing of the subduction of the Gran Paradiso Massif

Our new petrochronological data constrain the burial and exhumation of the Gran Paradiso and Money Units. Textural and chemical data suggest that, in the Gran Paradiso sample, the garnet rim and monazite grew coevally at peak metamorphic conditions (~60 km, 18–20 kbar, 500–520 °C,) at ~42 Ma. The Money Unit was buried at a slightly lower depth (~55 km, ~17 to 18 kbar, ~550 °C) than the Gran Paradiso Unit, and monazite gave an age of ~42 Ma for this episode. Therefore, we conclude that both units reached their maximal subduction depth contemporaneously ca. 42 Ma ago.

Previous studies indicate the timing of the HP metamorphism in the Gran Paradiso Unit either at 43.0 ± 0.5 Ma (Meffan-Main et al. 2004) or 33.7 ± 1.6 Ma (Radulescu et al. 2009). Both ages were obtained in metasomatic rocks (whiteschists): the former is based on a single Rb/Sr two-point isochron in a disequilibrium assemblage, whereas the latter is determined on allanite displaying an initial, inherited Pb with a complex isotopic composition. Without providing direct temporal constraints on the HP metamorphism, Rosenbaum et al. (2012) suggested that eclogite-facies metamorphism in the Gran Paradiso Unit took place prior to or at ~41 Ma. Likewise, as suggested by Rosenbaum et al. (2012), data for the present study also support a HP metamorphic event at ca. 42 Ma.

Other pieces of continental crust derived from the Briançonnais microcontinent and now exposed as tectonic windows through the oceanic units are represented by the Monte Rosa and Dora-Maira Massifs. In the Monte Rosa Massif, monazite ages from garnet paragneisses ranging from 46 to 31 Ma have been taken as an indication of the HP episode (Engi et al. 2001). More recently, dating on rutile from quartz–carbonate–white mica–rutile veins hosted within eclogite and schists from the Monte Rosa Massif provided well-constrained evidence of eclogite-facies metamorphism at 42.6 ± 0.6 Ma (Lapen et al. 2007). This age is in good agreement with geochronological data presented in the present study for HP metamorphism in the Gran Paradiso Massif. In the nearby

Gornergrat Unit, considered as either part of the Monte Rosa Massif (Rubatto and Gebauer 1999) or as an independent unit (Steck et al. 2015), four zircon rims from phengite-rich metaquartzite yield an age of ~35 Ma, interpreted as the age of HP metamorphism (Rubatto and Gebauer 1999).

In the Dora-Maira Massif, the notorious UHP Brossasco-Isasca Unit was buried at ~120 km at 35–33 Ma (e.g. Duchêne et al. 1997a; Gebauer et al. 1997; Rubatto and Hermann 2001; Di Vincenzo et al. 2006; Gauthiez-Putallaz et al. 2016). These ages are significantly younger than the ages obtained in our study, challenging the commonly argued idea that both units, the HP Gran Paradiso Unit and the UHP Brossasco-Isasca Unit, reached their maximum burial contemporaneously (Radulescu et al. 2009). This discrepancy in age may result from the fact that the HP Gran Paradiso Unit should not be compared to the UHP Brossasco-Isasca Unit, but rather to the HP units from the Dora-Maira Massif. However, these have not been dated accurately so far as Ar/Ar data on phengite from orthogneisses, micaschists (Scaillet et al. 1990) and eclogites (Scaillet 1996) are contaminated by excess argon.

Timing of the exhumation of the Gran Paradiso Massif

Thrusting of the Gran Paradiso on top of the Money Unit is responsible for the development of the main S_2 foliation (Manzotti et al. 2015b) and occurred once peak *P* conditions had been reached (at ~48 km depth, ~14 kbar, ~560 °C) in both units. Folding of the thrust took place during stage 3 (Manzotti et al. 2015b). *P*–*T* conditions for this stage have not been modelled. Based on the minerals (muscovite, chlorite, albite) defining the axial-plane schistosity in the few cases where it developed, we conclude that stage 3 may have occurred at epidote–amphibolite facies conditions (~35 km, ~10 kbar, ~520 to 550 °C). Static replacement of garnet by chlorite or biotite is ascribed to stage 4 (at ~22 to 30 km, ~6 to 8 kbar, ~500 °C), but may have also taken place during stage 3 in the domains, where a new foliation (S_3) did not develop. Because thrusting was achieved during stage 2, and folding of the thrust took place during stage 3, it follows that the Gran Paradiso and Money Units were no longer moving independently from each other, but were exhumed conjointly (Manzotti et al. 2014b, 2015b) and at the same rate. Geochronological data on xenotime associated with garnet breakdown into biotite indicate an age of ~32 Ma for stage 4 in the Gran Paradiso Unit.

Tectonic implications of the new age data

Exhumation rates

Burial and exhumation rates depend on the forces applied at the boundary of convergent systems and on the internal dynamics of the orogen (i.e., the driving forces leading to the exhumation of HP rocks, erosion and/or buoyancy) (e.g. Gerya et al. 2008; Yamato et al. 2008; Butler et al. 2013, 2014; Warren 2013; Schenker et al. 2015; Schmalholz and Schenker 2015). If subduction rates (of the order of 1 to 10 cm/year) are known from plate tectonic reconstructions (e.g., DeMets et al. 1994; Schellart et al. 2007), exhumation rates can be determined by linking isotopic ages to well-defined retrograde metamorphic paths (Duchêne et al. 1997b; Agard et al. 2009; Kylander-Clark et al. 2012).

Fast exhumation rates (i.e., of the order of 2–5 cm/year) have been mostly estimated for UHP units, such as the Brossasco-Isasca Unit in the Western Alps (Rubatto and Hermann 2001) and the Kokchetav Massif in Kazakhstan (Dobretsov et al. 1995; Shatsky et al. 1999; Hermann et al. 2001). Carswell et al. (2003) estimate an exhumation rate on the order of 1 cm/year for the Western Gneiss Region of Norway. However, exhumation rates for this region are still disputed and slower rates (c. 7 mm/year) have been proposed by Kylander-Clark et al. (2008). Similar rates are estimated in the Tso Morari Dome (e.g., de Sigoyer et al. 2000, 2004; Schlup et al. 2001; Epard and Steck 2008, St-Onge et al. 2013).

In the Western Alps, geochronologists have now established that the HP stage is diachronous at the scale of the mountain belt (e.g., Duchêne et al. 1997a; Regis et al. 2014a, b). Few studies have tried to estimate burial and exhumation rates, mainly in UHP metamorphic rocks (e.g., exhumation rates of ~34 mm/year, Rubatto and Hermann 2001). The difference in ages between the peak *P* (typically eclogite-facies) and the lower *P* overprint (typically greenschist-facies) has been estimated either by combining different isotopic methods (e.g. Gebauer et al. 1997) or using the same method on a specific mineral grown at different *P*–*T* conditions (e.g., titanite: Rubatto and Hermann 2001).

For the Gran Paradiso Unit, preliminary estimates in the range of 20 and 12 mm/year have been suggested for a first and second stage of exhumation (Fig. 13), respectively (Radulescu et al. 2009). These values have been obtained by combining different isotopic methods (Rb–Sr data from Freeman et al. 1997; zircon and apatite fission-track data from Malusà et al. 2005; Malusà and Vezzoli 2006, and U–Pb data from Radulescu et al. 2009), applied to different samples collected in different areas.

Our study, based on micro-textural, petrological and U–Th–Pb geochronological investigations on two samples, indicates that the *P* peak (stage 1) took place at c. 42 Ma (41.5 ± 0.3, 42.0 ± 0.6 Ma, in the Gran Paradiso and Money Units, respectively; Fig. 12). Retrogression under greenschist-facies conditions, recorded by biotite replacement of garnet (stage 4), has been dated at 32.3 ± 1.0 Ma (our xenotime age). Consequently, the thrusting of the Gran Paradiso Unit over the Money Unit (stage 2) took place in the interval

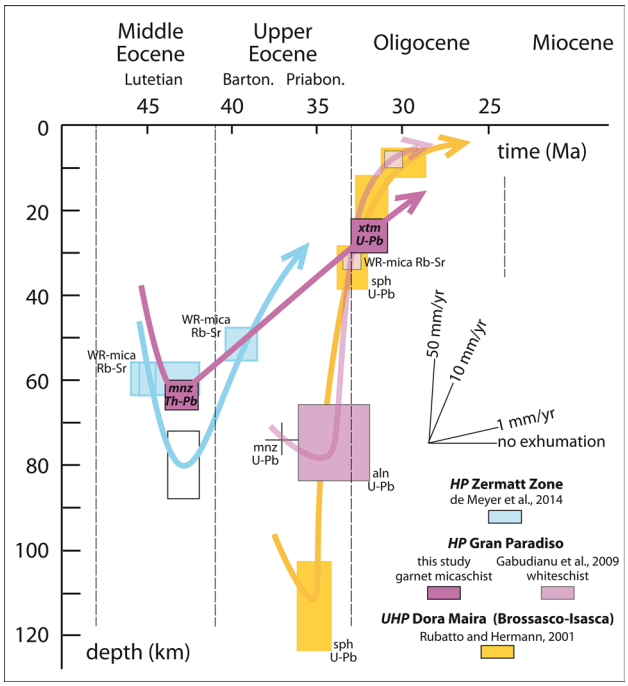

Fig. 13 Depth vs. time paths from which the mean exhumation rates are calculated. The conversion from pressure to depth was calculated by assuming a 20-km-thick upper crust and a 10-km-thick lower crust followed by an upper mantle with densities of 2.7, 3.0, and 3.3 g/cm^3, respectively. In this model, a minimum crustal thickness of 30 km for the upper plate is assumed, because the subduction of the Gran Paradiso Unit occurred before continental collision. Any increase in crustal thickness would lead to a slight increase in subduction depth and hence to higher exhumation rates

between 42 and 32 Ma, and the exhumation (from 20 to c. 6–8 kbar) took about 10 Ma. For the sake of comparison, we follow Rubatto and Hermann's (2001) approach to convert pressure into depth and to calculate the exhumation rates for the Gran Paradiso Unit: a 20-km-thick upper crust, a 10-km-thick lower crust, followed by an upper mantle with densities of 2.7, 3.0 and 3.3 g/cm^3, respectively. On the basis of these assumptions and considering a lithostatic pressure, our data suggest average exhumation rates of the order of 2.2 mm/year (2.2 km/Ma) to 5 mm/year (5 km/Ma) (Fig. 13). These values are considerably lower than the previous ones proposed for the Gran Paradiso Unit (Radulescu et al. 2009), but within the same range as those estimated for the Schistes Lustrés (1–2 mm/year, Agard et al. 2002).

Exhumation mechanism

The exhumation mechanism of HP and UHP rocks has been debated for many years (e.g., Platt 1993; Brun and Faccenna 2008; Agard et al. 2009; Butler et al. 2013; Warren 2013; Burov et al. 2014; Schenker et al. 2015). A detailed discussion of this topic in the Alpine Belt is outside the scope of this paper. However, the implications of our geochronological data deserve a brief discussion in this context. Most researchers agree that erosion alone cannot account for the exhumation of HP rocks, as shown by mass-balance estimates of eroded volumes and sediment deposition in foreland basins (e.g., Malusà et al. 2011). In addition to erosion, a tectonic mechanism is required, for which several possibilities have been envisioned. To clarify our view, we propose a geometrical and kinematical model of the evolution in the Western Alps (Fig. 14), partly similar to those presented by other authors (e.g., Rosenbaum et al. 2012; Steck et al. 2015), but which differs in terms of the mechanism responsible for the exhumation process. Before its involvement in the convergence zone, the Briançonnais microcontinent was located between the Piemonte-Liguria Ocean to the east and the Valaisan Basin to the west. Because the Gran Paradiso Unit only displays upper crustal rocks, it is probable that it represents the most distal part of the palaeomargin, characterized by upper crustal blocks detached from their lower crustal counterpart during the Jurassic extension (Fig. 14a). During the early stages of its subduction, the distal part of the Briançonnais palaeomargin remained largely consistent, and the more distal part (i.e., the Gran Paradiso Unit) was equilibrating at greater depths (hence *P*) than the more proximal part (i.e., the Money Unit). In both units, peak *P* assemblages (stage 1) are dated at about 42 Ma (Fig. 14b). These peak *P* assemblages actually record the depth and timing at which the detachment of these crustal units from the downgoing slab occurred.

During the subduction of the Briançonnais microcontinent, the detachment of crustal slices led to the thrusting of more internal units (i.e., higher *P*) over more external (i.e., lower *P*) units (Fig. 14c), recorded in the studied area by the thrusting of the Gran Paradiso Unit over the Money Unit (stage 2). Our geochronological data can be used to bracket the age of this event at roughly 40–35 Ma. Thrusting is accompanied by exhumation of the nappe stack, because it occurred at decreasing *P* in both the footwall (Money) and hangingwall (Gran Paradiso). It is, therefore, possible to define an extruding wedge, defined geometrically by an upper shear zone (the Combin Fault: Ballèvre and Merle 1993; Reddy et al. 1999; Rosenbaum et al. 2012) and an evolving lower shear zone, consisting of westward propagating thrusts. The extruding wedge consists of oceanic units detached from the downgoing slab (the Zermatt Zone) coupled with the subducted continental units, the latter having also (and possibly slightly later) been detached from the downgoing continental palaeomargin. According to the available age data, there is no significant difference in age for the eclogite-facies event in the Zermatt Zone (e.g., de Meyer et al. 2014) compared to the ages reported in this study for peak *P* assemblages in the Gran Paradiso and Money Units, at

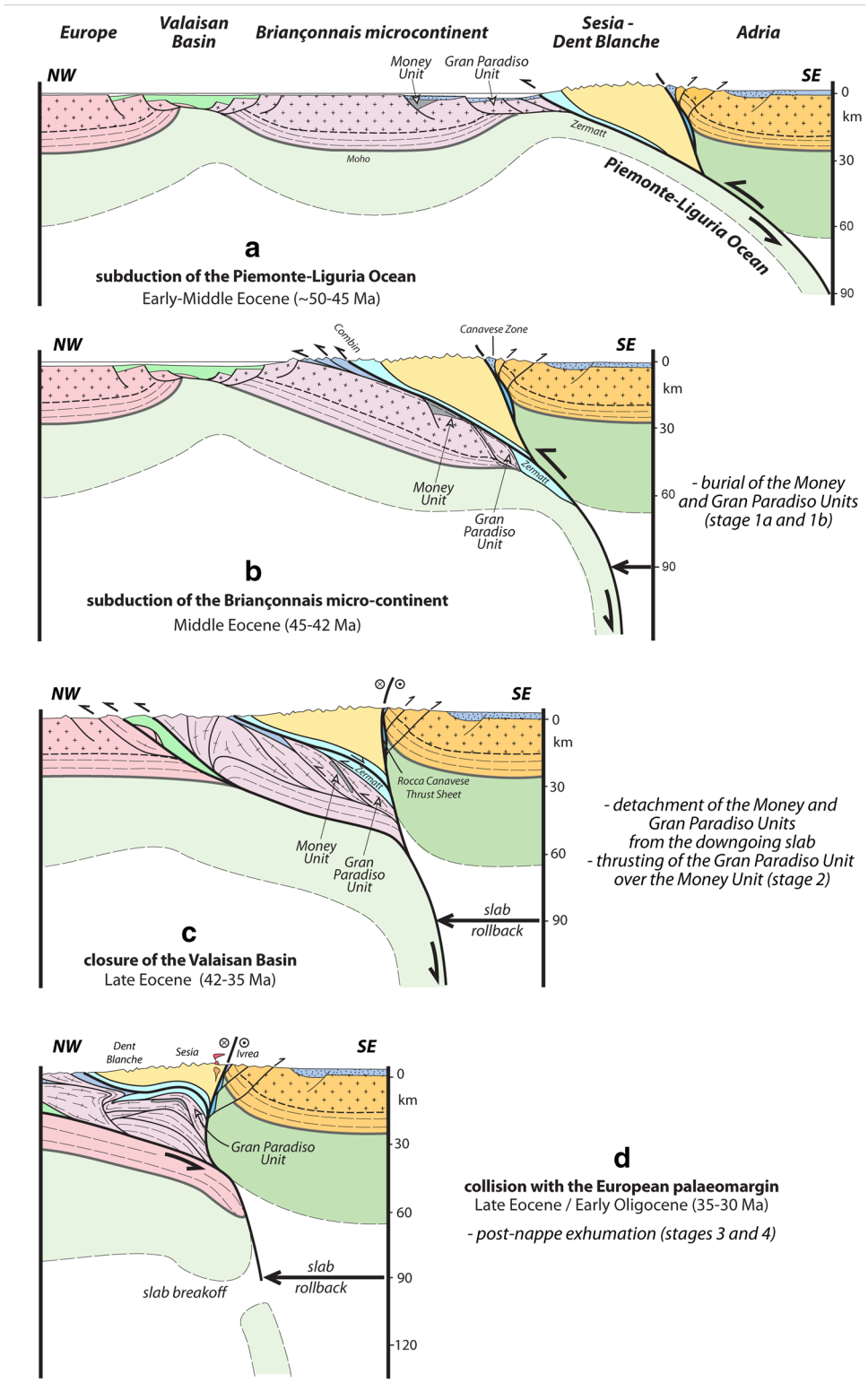

Fig. 14 Schematic evolution of the Alpine belt along the studied traverse. This reconstruction focuses on the Gran Paradiso and Money Units, based on the new geochronological data obtained in this study, indicating the subduction of the Briançonnais microcontinent at about 42 Ma. Details about the tectonic history of the Sesia-Dent Blanche nappes may be found in Manzotti et al. (2014a)

about 42 Ma. This means that subduction of the oceanic units and the distal part of the Briançonnais palaeomargin was nearly synchronous, and that the timing of the detachment of the oceanic and continental units from the downgoing slab is within error of the available geochronological data.

The driving force or the upward movement of the extruding wedge is a matter of debate. In our scheme (Fig. 14), we assumed that a slab rollback of the downgoing plate was occurring during the same time interval as when the building of the nappe stack was taking place in the deepest part of the orogen, i.e., in the extruding wedge. However, we also assumed that the slab rollback rate is nearly equal to the convergence rate between the European and Adriatic plates, allowing upward displacement of the extruding wedge, but excluding significant crustal extension in the upper plate; a major difference with respect to the classic Apennine and Aegean examples (Brun and Faccenna 2008).

Displacement along the thrusts separating the Money and Gran Paradiso nappes ceased during and after stage 3. Once the extruding wedge was closer to the surface, convergence continued, and the entire extruding wedge was folded due to the westward propagation of the Adriatic indenter (Schmid et al. 2017) (Fig. 14d). The Valaisan suture and its continuation below our study area to the base of the Ivrea mantle wedge represents a major decoupling plane between the European plate in the footwall and the already exhumed HP–UHP nappe stack in the hangingwall. In the latter, northwestward displacement along the Valaisan suture is accompanied by upright to east-verging folding of the previous orogenic wedge, the resulting antiformal stack deforming the 'normal shear sense' Combin Fault on top and the lower thrusts at the base of the wedge (Fig. 14d). Slab rollback may have continued after this stage, controlling to some extent the development of the foreland basin at the front of the westward propagating orogenic wedge (Schlunegger and Kissling 2015).

Conclusions

1. For the first time ever, the exhumation of a HP unit (i.e., the Gran Paradiso Unit) is described by three *P–T–t* points, all obtained by applying the same dating technique (in situ and in context LA-ICP-MS) on three different geochronometers (monazite, xenotime and allanite) from the same sample. Peak *P* values (~ 18 to 20 kbar) were attained at c. 42 Ma, while retrogression at ~ 10 kbar was achieved at about 32 Ma.
2. In the underlying Money Unit, peak *P* (~ 17 to 18 kbar) was also reached at c. 42 Ma, i.e., at the same time as in the Gran Paradiso Unit. Thrusting took place at ~ 14 kbar before the final retrogression in the Gran Paradiso Unit, dated at c. 32 Ma.
3. These data are consistent with a geometrical–kinematical model involving subduction of the Briançonnais microcontinent at 42 Ma, shortly after or contemporaneous with the subduction of the Piemonte-Liguria Ocean (e.g., de Meyer et al. 2014). The widespread occurrence of ductile deformation along the main tectonic boundaries separating the Gran Paradiso Unit and Piemonte-Liguria Ocean suggests that stacking of the oceanic units over the Gran Paradiso Unit likely occurred during an early stage of the exhumation process, at a minimum depth of 40 km.
4. The stacking of the Gran Paradiso Unit over a more external part of the Briançonnais microcontinent, the Money Unit, involves thrust propagation towards more external zones, before folding of the nappe stack and coeval exhumation at c. 32 Ma.
5. Average exhumation rates for the studied area are at about 2.2–5 mm/year, a value one order of magnitude lower than those found in other HP–UHP units in the Western Alps (Rubatto and Hermann 2001), but similar to those obtained in the "Schistes Lustrés Complex" (Agard et al. 2002).

Acknowledgements This work was financially supported by the Swiss National Science Foundation (Project PZ00P2_161202). 'Ente Parco Nazionale Gran Paradiso' is thanked for allowing fieldwork and rock sampling in the Valnontey valley. 'Villaggio Alpino Don Bosco' is thanked for providing accommodation at the Alpe Money hut. X. Le Coz and L. Nicod are acknowledged for making the numerous thin sections required for our study on the Gran Paradiso Massif. We thank P. Vonlanthen for help in using the SEM and J.-L. Devidal for help with the EMPA analyses on the accessory phases. We are grateful to D. Tinkham for making available the conversion of the THERMOCALC mixing models for the Theriak-Domino software. We have much appreciated discussions and exchanges with L.P. Baumgartner, S. Schmalholz and J.P. Brun. We thank also Dr. Sara Mullin for revising our English language. Finally, K. Mottram and an anonymous reviewer are thanked for their constructive and helpful reviews which significantly improved this paper. The careful editorial work of S. Reddy is gratefully acknowledged.

References

Agard P, Monié P, Jolivet L, Goffé B (2002) Exhumation of the Schistes Lustrés complex: in situ laser probe $^{40}Ar/^{39}Ar$ constraints and implications for the Western Alps. J Metamorph Geol 20:599–618

Agard P, Yamato P, Jolivet L, Burov E (2009) Exhumation of oceanic blueschist and eclogites in subduction zones: timing and mechanisms. Earth Sci Rev 92:53–79

Andersen TB, Jamtveit B, Dewey JF, Swensson E (1991) Subduction and eduction of continental crust: major mechanisms during continent-continent collision and orogenic collapse, a model based on the south Norwegian Caledonides. Terra Nova 3:303–310

Argand E (1924) La tectonique de l'Asie. XIIIème Congrès Géologique International (Bruxelles). Comptes-rendus 1:171–372

Ashley KT, Steele-MacInnis M, Caddick MJ (2014) QuiB Calc: A MATLAB® script for geobarometry based on Raman spectroscopy and elastic modeling of quartz inclusions in garnet. Comput Geosci 66:155–157

Babist J, Handy MR, Konrad-Schmolke M, Hammerschmidt K (2006) Precollisional, multistage exhumation of subducted continental

crust: The Sesia Zone, western Alps. Tectonics 25:TC6008. https://doi.org/10.1029/2005TC001927

Ballèvre M, Merle O (1993) The Combin Fault: compressional reactivation of a Late Cretaceous-Early Tertiary detachment fault in the Western Alps. Schweiz Mineral Petrog Mittei 73:205–227

Bertrand JM, Paquette JL, Guillot F (2005) Permian zircon U–Pb ages in the Gran Paradiso massif: revisiting post-Variscan events in the Western Alps. Schweiz Mineral Petrog Mittei 85:15–29

Beyssac O, Goffé B, Chopin C, Rouzaud JN (2002) Raman spectra of carbonaceous material in metasediments: a new geothermometer. J Metamorph Geol 20:859–871

Beyssac O, Goffé B, Petitet JP, Froigneux E, Moreau M, Rouzaud JN (2003) On the characterization of disordered and heterogeneous carbonaceuous materials using Raman spectroscopy. Spectrochimica Acta A 59:2267–2276

Brun JP, Faccenna C (2008) Exhumation of high-pressure rocks driven by slab rollback. Earth Planet Sci Lett 272:1–7

Burov E, Francois T, Agard P, Le Pourhiet L, Meyer B, Tirel C, Lebedev S, Yamato P, Brun J-P (2014) Rheological and geodynamic controls on the mechanisms of subduction and HP/UHP exhumation of crustal rocks during continental collision: insights from numerical models. Tectonophysics 631:212–250

Butler JP, Beaumont C, Jamieson RA (2013) The Alps 1: a working geodynamic model for burial and exhumation of (ultra)high-pressure rocks in Alpine-type orogens. Earth Planet Sci Lett 377–378:114–131

Butler JP, Beaumont C, Jamieson RA (2014) The Alps 2: controls on crustal subduction and (ultra)high-pressure rock exhumation in Alpine-type orogens. J Geophy Res Solid Earth 119:5987–6022

Carignan J, Hild P, Mevelle G, Morel J, Yeghicheyan D (2001) Routine analyses of trace elements in geological samples using flow injection and low pressure on-line liquid chromatography coupled to ICP-MS: a study of geochemical reference materials, BR, DRN, UB-N, AN-G and GH. Geostandards Newslett 25:187–198

Carswell DA, Brueckner HK, Cuthbert SJ, Mehta K, O'Brien PJ (2003) The timing of stabilisation and the exhumation rate for ultra-high pressure rocks in the Western Gneiss Region of Norway. J Metamorph Geol 21:602–612

Compagnoni R, Elter G, Lombardo B (1974) Eterogeneita stratigrafica del complesso degli «gneiss minuti» nel massicio cristallino del Gran Paradiso. Mem Soc Geol Ital Supplemento 13:227–239

Dal Piaz GV, Lombardo B (1986) Early Alpine eclogite metamorphism in the Penninic Monte Rosa-Gran Paradiso basement of the northwestern Alps. In: Evans BW, Brown EH (eds) Blueschists and eclogites, vol 164. Geol Soc Amer Mem, Boulder, CO, pp 249–265

de Capitani C, Brown TH (1987) The computation of chemical equilibrium in complex systems containing non-ideal solutions. Geochim Cosmochim Acta 51:2639–2652

de Capitani C, Petrakakis K (2010) The computation of equilibrium assemblage diagrams with Theriak/Domino software. Am Mineral 95:1006–1016

de Sigoyer J, Chavagnac V, Blichert-Toft J, Villa IM, Luais B, Guillot S, Cosca M, Mascle G (2000) Dating the Indian continental subduction and collisional thickening in the northwest Himalaya: multichronology of Tso Morari eclogites. Geology 28:487–490

de Sigoyer J, Guillot S, Dick P (2004) Exhumation rate of the ultrahigh-pressure Tso Morari unit in eastern Ladakh (NW Himalaya): a case study. Tectonics 23:TC3003

de Meyer CMC, Baumgartner LP, Beard BL, Johnson CM (2014) Rb–Sr ages from phengite inclusions in garnets from high pressure rocks of the Swiss Western Alps. Earth Planet Sci Lett 395:205–216

DeMets C, Gordon RG, Argus DF, Stein S (1994) Effect of recent revisions to the geomagnetic reversal time scale on estimates of current plate motions. Geophys Res Lett 21:2191–2194

Dewey JF, Bird JM (1970) Mountain belts and the new global tectonics. J Geophys Res 75:2625–2647

Di Vincenzo G, Tonarini S, Lombardo B, Castelli D, Ottolini L (2006) Comparison of 40Ar–39Ar and Rb–Sr data on phengites from the UHP Brossasco-Isasca Unit (Dora Maira Massif, Italy): implications for dating white mica. J Petrol 47:1439–1465

Dobretsov NL, Sobolev NL, Shatsky VS, Coleman RG, Ernst WG (1995) Geotectonic evolution of diamondiferous parageneses Kokchetav Complex, Northern Kazakhstan – the geologic enigma of ultrahigh-pressure crustal rocks within Phanerozoic foldbelt. Isl Arc 4:267–279

Duchêne S, Blichert-Toft J, Luais B, Télouk P, Lardeaux J-M, Albarède F (1997a) The Lu–Hf dating of garnets and the ages of the Alpine high-pressure metamorphism. Nature 387:586–589

Duchêne S, Lardeaux J-M, Albarède F (1997b) Exhumation of eclogites: insights from depth-time path analysis. Tectonophysics 280:125–140

Engi M, Scherrer NC, Burri T (2001) Metamorphic evolution of pelitic rocks of the Monte Rosa nappe: constraints from petrology and single grain monazite age data. Schweiz Mineral Petrog Mitt 81:305–328

Epard JL, Steck A (2008) Structural development of the Tso Morari ultra-high pressure nappe of the Ladakh Himalaya. Tectonophysics 451:242–264

Fitzsimons I, Kinny P, Wetherley S, Hollingsworth D (2005) Bulk chemical control on metamorphic monazite growth in pelitic schists and implications for U–Pb age data. J Metamorph Geol 23:261–277

Freeman SR, Inger S, Butler RWH, Cliff RA (1997) Dating deformation using Rb–Sr in white mica: greenschist facies deformation ages from the Entrelor shear zone, Italian Alps. Tectonics 16:55–76

Gasco I, Borghi A, Gattiglio M (2010) Metamorphic evolution of the Gran Paradiso Massif: a case study of an eclogitic metagabbro and a polymetamorphic glaucophane–garnet micaschist. Lithos 115:101–120

Gauthiez-Putallaz L, Rubatto D, Hermann J (2016) Dating prograde fluid pulses during subduction by in situ U–Pb and oxygen isotope analysis. Contrib Mineral Petrol 171:15

Gebauer D, Schertl HP, Brix M, Schreyer W (1997) 35 Ma old ultrahigh-pressure metamorphism and evidence for very rapid exhumation in the Dora Maira Massif, Western Alps. Lithos 41:5–24

Gerya TV, Perchuk LL, Burg JP (2008) Transient hot channels: Perpetrating and regurgitating ultrahigh-pressure, high-temperature crust-mantle associations in collision belts. Lithos 103:236–256

Grand'Homme A, Janots E, Seydoux-Guillaume AM, Guillaume D, Bosse V, Magnin V (2016) Partial resetting of the U–Th–Pb systems in experimentally altered monazite: nanoscale evidence of incomplete replacement. Geology 44:431–434

Groppo C, Castelli D, Compagnoni R (2006) Late chloritoid–staurolite assemblage in a garnet–kyanite-bearing metapelite from the ultrahigh-pressure Brossasco-Isasca unit (Dora-Maira Massif, Western Alps): new petrological constraints for a portion of the decompressional path. Geol Soc Spec Pap 403:127–138

Groppo C, Beltrando M, Compagnoni R (2009a) The P–T path of the ultra-high pressure Lago di Cignana and adjoining high-pressure meta-ophiolitic units: insights into the evolution of the subducting Tethyan slab. J Metamorph Geol 27:207–231

Groppo C, Rolfo F, Lombardo B (2009b) P–T evolution across the Main Central Thrust Zone (Eastern Nepal): hidden discontinuities revealed by petrology. J Petrol 50:1149–1180

Guiraud M, Powell R (2006) P–V–T relationships and mineral equilibria in inclusions in minerals. Earth Planet Sci Lett 244:683–694

Guiraud M, Powell R, Rebay G (2001) H_2O in metamorphism and unexpected behaviour in the preservation of metamorphic mineral assemblages. J Metam Geol 19:445–454

Henry DJ, Guidotti CV, Thomson JA (2005) The Ti-saturation surface for low-to-medium pressure metapelitic biotites: implications for geothermometry and Ti-substitution mechanisms. Am Min 90:316–328

Hermann J, Rubatto D, Korsakov A, Shatsky VS (2001) Multiple zircon growth during fast exhumation of diamondiferous, deeply subducted continental crust (Kokchetav Massif, Kazakhstan). Contrib Mineral Petrol 141:66–82

Holland TJB, Powell R (1998) An internally consistent thermodynamic data set for phases of petrological interest. J Metamorph Geol 16:309–343

Hurford AJ, Hunziker JC (1989) A revised thermal history for the Gran Paradiso massif. Schweiz Mineral Petrog Mitt 69:319–329

Johnson RW, Harley SL (2012) Orogenesis. The making of mountains. Cambridge University Press, Cambridge

Kohn M (2014) "Thermo-Raman-try": Calibration of spectroscopic barometers and thermometers for mineral inclusions. Earth Planet Sci Let 388:187–196

Kohn M, Engi M, Lanari P (2017) Petrochronology: methods and applications. Rev Mineral Geoch, Chantilly, VA, p 83

Kylander-Clark ARC, Hacker BR, Mattinson JM (2008) Slow exhumation of UHP terranes: titanite and rutile ages of the Western Gneiss Region, Norway. Earth Planet Sci Lett 272:531–540

Kylander-Clark ARC, Hacker BR, Mattinson CG (2012) Size and exhumation rate of ultrahigh-pressure terranes linked to orogenic stage. Earth Planet Sci Lett 321–322:115–120

Lapen TJ, Johnson CM, Baumgartner LP, Dal Piaz GV, Skora S, Beard BL (2007) Coupling of oceanic and continental crust during Eocene eclogite-facies metmorphism: evidence from the Monte Rosa nappe, western Alps. Contrib Mineral Petrol 153:139–157

Le Bayon B, Ballèvre M (2004a) Field and petrological evidence for a late Palaeozoic (Permian) age of the Erfaulet oorthogneiss. CR Geosci 336:1079–1089

Le Bayon B, Ballèvre M (2004b) Field and petrological evidence for a late Palaeozoic (Permian) age of the Erfaulet orthogneiss. CR Geoscience 336:1079–1089

Le Bayon B, Ballèvre M (2006) Deformation history of a subducted continental crust (Gran Paradiso, Western Alps): continuing crustal shortening during exhumation. J Structural Geol 28:793–815

Le Bayon B, Pitra P, Ballèvre M, Bohn M (2006) Reconstructing P–T paths during continental collision using multi-stage garnet (Gran Paradiso nappe, Western Alps). J Metam Geol 24:477–496

Leake BE, Woolley AR, Arps CES, Birch WD, Gilbert MC, Grice JD, Hawthorne FC, Kato A, Kisch HJ, Krivovichev VG, Linthout K, Laird J, Maresch WV, Nickel EH, Rock NMS (1997) Nomenclature of amphiboles. Report of the subcommittee on amphiboles of the international mineralogical association commission on new minerals and mineral names. Eur J Mineral 9:623–651

López-Carmona A, Pitra P, Abati J (2013) Blueschist-facies metapelites from Malpica-Tui Unit (NW Iberian Massif): phase equilibria modelling and H_2O and Fe_2O_3 influence in high-pressure assemblages. J Metamorph Geol 31:263–280

Malusà MG, Vezzoli G (2006) Interplay between erosion and tectonics in the Western Alps. Terra Nova 18:104–108

Malusà MG, Polino R, Zattin M, Bigazzi G, Martin S, Piana F (2005) Miocene to present differential exhumation in the Western Alps: insights from fission-track thermochronology. Tectonics 24:1–23

Malusà MG, Faccenna C, Garzanti E, Polino R (2011) Divergence in subduction zones and exhumation of high pressure rocks (Eocene Western Alps). Earth Planet Sci Lett 310:21–32

Manzotti P, Ballèvre M (2013) Multi-stage garnet in high-pressure metasediments: Alpine overgrowths on Variscan detrital grains. Geology 41:1151–1154

Manzotti P, Ballèvre M, Zucali M, Robyr M, Engi M (2014a) The tectonometamorphic evolution of the Sesia-Dent Blanche nappes (internal Western Alps): review and synthesis. Swiss J Geosci 107:309–336

Manzotti P, Le Carlier de Veslud C, Le Bayon B, Ballèvre M (2014b) Petro-structural map of the Money Unit (Gran Paradiso Massif, Valnontey valley, Western Alps). J Maps 10:324–340

Manzotti P, Poujol M, Ballèvre M (2015a) Detrital zircon in blueschist-facies-metaconglomerates from the Western Alps: implications for the late Carboniferous to early Permian palaeogeography. Int J Earth Sci 104:703–731

Manzotti P, Pitra P, Langlade J, Ballèvre M (2015b) Constraining P–T conditions during thrusting of a higher pressure unit over a lower pressure one (Gran Paradiso, Western Alps). J Metamorph Geol 33:981–1002

Massonne HJ (2015) Derivation of P–T paths from high-pressure metagranites—examples from the Gran Paradiso Massif, Western Alps. Lithos 226:265–279

Meffan-Main S, Cliff RA, Barnicoat AC, Lombardo B, Compagnoni R (2004) A Tertiary age for Alpine high-pressure metamorphisms in the Gran Paradiso massif, Western Alps: a Rb–Sr microsampling study. J metamorph Geol 22:267–281

Perchuk LL (1991) Derivation of a thermodynamically consistent set of geothermometers and geobarometers for metamorphic and magmatic rocks. In: Perchuk LL (ed) Progress in metamorphic and magmatic petrology, a memorial volume in honor of DS Korzhinskiy. Cambridge Univ Press, Cambridge, pp 93–112

Petrík I, Broska I, Lipka J, Siman P (1995) Granitoid allanite-(Ce): substitution relations redox conditions and REE distributions (on an example of I-type granitoids, western Carpathians, Slovakia). Geol Carpath 46:79–94

Pfiffner OA (2014) Geology of the Alps. Wiley-Blackwell, Oxford, 376p

Pitra P, Kouamelan AN, Ballèvre M, Peucat JJ (2010) Palaeoproterozoic high-pressure granulite overprint of the Archean continental crust: evidence for homogeneous crustal thickening (Man Rise, Ivory Coast). J Metamorph Geol 28:41–58

Platt JP (1993) Exhumation of high-pressure rocks: a review of concepts and processes. Terra Nova 5:119–133

Powell R, Holland TJB (1988) An internally consistent dataset with uncertainties and correlations: 3. Applications to geobarometry, worked examples and a computer program. J Metamorph Geol 6:173–204

Proyer A (2003) The preservation of high-pressure rocks during exhumation: metagranites and metapelites. Lithos 70:183–194

Pyle JM, Spear FS (1999) Yttrium zoning in garnet: coupling of major and accessory phases during metamorphic reactions. Geol Mat Res 1:1–49

Radulescu IG, Rubatto D, Gregory C, Compagnoni R (2009) The age of HP metamorphism in the Gran Paradiso Massif, Western Alps: a petrological and geochronological study of "silvery micaschists". Lithos 110:95–108

Reddy SM, Wheeler J, Cliff RA (1999) The geometry and timing of orogenic extension: an example from the Western Italian Alps. J Metam Geol 17:573–589

Regis D, Rubatto D, Darling J, Cenki-Tok B, Zucali M, Engi M (2014a) Multiple metamorphic stages within an eclogite-facies terrane (Sesia Zone, Western Alps) revealed by Th–U–Pb petrochronology. J Petrol 55:1429–1456

Regis D, Warren CJ, Young D, Roberts NMW (2014b) Tectono-metamorphic evolution of the Jomolhari massif: variations in timing of syn-collisional metamorphism across western Bhutan. Lithos 190:449–466

Regis D, Warren CJ, Mottram CM, Roberts NMW (2016) Using monazite and zircon petrochronology to constrain the *P–T–t* evolution of the middle crust in the Bhutan Himalaya. J Metam Geol 34:617–639

Ring U, Collins AS, Kassem OK (2005) U–Pb SHRIMP data on the crystallization age of the Gran Paradiso augengneiss, Italian Western Alps: Further evidence for Permian magmatic activity in the Alps during break-up of Pangea. Eclogae Geol Helv 98:363–370

Rosenbaum G, Menegon L, Glodny J, Vasconcelos P, Ring U, Massironi M, Thiede D, Nasipuri P (2012) Dating deformation in the Gran Paradiso Massif (NW Italian Alps): Implications for the exhumation of high-pressure rocks in an collisional belt. Lithos 144–145:130–134

Rubatto D, Gebauer D (1999) Eo/Oligocene (35 Ma) high-pressure metamorphism in the Gornegrat Zone (Monte Rosa, Western Alps): implications for paleogeography. Schweiz Mineral Petrog Mittei 79:353–362

Rubatto D, Hermann J (2001) Exhumation as fast as subduction? Geology 29:3–6

Scaillet S (1996) Excess ^{40}Ar transport scale and mechanism in high-pressure phengites: a case study from an eclogitized metabasite of the Dora-Maira nappe, western Alps. Geochim Cosmochim Acta 60:1075–1090

Scaillet S, Féraud G, Lagabrielle Y, Ballèvre M, Ruffet G (1990) ^{40}Ar/^{39}Ar laser-probe dating by step-heating and spot-fusion of phengites from the Dora-Maira nappe of the western Alps, Italy. Geology 18:741–744

Schärer U (1984) The effect of initial ^{230}Th disequilibrium on young U–Pb ages: the Makalu case, Himalaya. Earth Planet Sci Lett 67:191–204

Schellart WP, Freman J, Stegman DR, Moresi L, May D (2007) Evolution and diversity of subduction zones controlled by slab width. Nature 446:308–311

Schenker FL, Schmalholz SM, Moulas E, Pleuger J, Baumgartner LP, Podladchikov Y, Vrijmoed J, Buchs N, Müntener O (2015) Current challenges for explaining (ultra)high-pressure tectonism in the Pennine domain of the Central and Western Alps. J Metamorph Geol 33:869–886

Schlunegger F, Kissling E (2015) Slab rollback orogeny in the Alps and evolution of the Swiss Molasse basin. Nat Commun 6:8605. https://doi.org/10.1038/ncomms9605

Schlup M, Carter A, Steck A (2001) Exhumation history revealed by fission track cooling ages in the North Himalayan Crystalline zone of eastern Ladakh, NW Himalaya. J Asian Earth Sci 19:57–58

Schmalholz SM, Schenker FL (2015) Exhumation of the Dora Maira ultrahigh-pressure unit by buoyant uprise within a low-viscosity mantle oblique-slip shear zone. Terra Nova 28:348–355

Schmid SM, Fügenschuh B, Kissling E, Schuster R (2004) Tectonic map and overall architecture of the Alpine orogeny. Eclogae Geol Helv 97:93–117

Schmid SM, Kissling E, Diehl T, van Hinsberger DJJ, Molli G (2017) Ivrea mantle wedge, arc of the western Alps, and kinematic evolution of the Alps-Apennines orogenic system. Swiss J Geoscience. https://doi.org/10.1007/s0015-016-0237-0

Shatsky VS, Jagoutz E, Sobolev NV, Kozmenko OA, Parkhomenko VS, Troesch M (1999) Geochemistry and age of ultrahigh pressure metamorphic rocks from the Kokchetav massif (Northern Kazakhstan). Contrib Mineral Petrol 137:185–205

Smith HA, Barreiro (1990) Monazite U–Pb dating of staurolite grade metamorphism in pelitic schists. Contrib Mineral Petrol 105:602–615

Spear FS (2010) Monazite–allanite phase relations in metapelites. Chem Geol 279(1–2):55–62

Spear FS, Pyle JM (2002) Apatite, monazite, and xenotime in metamorphic rocks. Rev Mineral Geochem 48:295–335

Stacey JS, Kramers JD (1975) Approximation of terrestrial lead evolution by a two-stage model. Earth Planet Sci Lett 26:207–221

Steck A, Masson H, Robyr M (2015) Tectonics of the Monte Rosa and surrounding nappes (Switzerland and Italy): Tertiary phases of subduction, thrusting and folding in the Pennine Alps. Swiss J Geosci 108:3–34

St-Onge MR, Rayner N, Palin RM, Searle MP, Waters DJ (2013) Integrated pressure–temperature–time constraints for the Tso Morari dome (Northwest India): implications for the burial and exhumation path of UHP units in the western Himalaya. J Metamorph Geol 31:469–504

Sun SS, McDonough WF (1989) Chemical and isotopic systematics of oceanic basalts: implications for mantle composition and processes. In: Saunders AD, Norry MJ (eds) Magmatism in ocean basins, vol 42. Geol Soc London Spec Publ, London, pp 313–345

Taylor RJM, Clark C, Harley SL, Kylander-Clark ARC, Hacker BR, Kinny PD (2017) Interpreting granulite facies events through rare earth element partitioning arrays. J Metamorph Geol. https://doi.org/10.1111/jmg.12254

Thompson AB, Connolly JAD (1990) Metamorphic fluids and anomalous porosities in the lower crust. Tectonophysics 182:47–55

Vernon RH (2004) A practical guide to rock microstructure. Cambridge University Press, Cambridge, p 594

Warren CJ (2013) Exhumation of (ultra-)high-pressure terranes: concepts and mechanisms. Solid Earth 4:75–92

Yamato P, Burov E, Agard P, Le Pourhiet L, Jolivet L (2008) HP–UHP exhumation during slow continental subduction: self-consistent thermodynamically and thermomechanically coupled model with application to the Western Alps. Earth Planet Sci Lett 271:63–74

Yang P, Rivers T (2001) Chromium and manganese zoning in pelitic garnet and kyanite: spiral, overprint, and oscillatory (?) zoning patterns and the role of growth rate. J Metamorph Geol 19:455–574